Comprehensive symmetric-hybrid ring design for a proton EDM experiment at below 10^{-29} e · cm

Zhanibek Omarov,[1,2] Hooman Davoudiasl,[3] Selcuk Hacıömeroğlu,[2,*] Valeri Lebedev,[4] William M. Morse,[5] Yannis K. Semertzidis,[2,1,†] Alexander J. Silenko,[6,7,8] Edward J. Stephenson,[9] and Riad Suleiman[10]

[1]*Department of Physics, KAIST, Daejeon 34141, Republic of Korea*
[2]*Center for Axion and Precision Physics Research, IBS, Daejeon 34051, Republic of Korea*
[3]*High Energy Theory Group, Physics Department, Brookhaven National Laboratory, Upton, New York 11973, USA*
[4]*Fermi National Accelerator Laboratory, Batavia, Illinois 60510, USA*
[5]*Brookhaven National Laboratory, Upton, New York 11973, USA*
[6]*Bogoliubov Laboratory of Theoretical Physics, Joint Institute for Nuclear Research, Dubna 141980, Russia*
[7]*Institute of Modern Physics, Chinese Academy of Sciences, Lanzhou 730000, China*
[8]*Research Institute for Nuclear Problems, Belarusian State University, Minsk 220030, Belarus*
[9]*CEEM, Indiana University, Bloomington, Indiana 47408, USA*
[10]*Thomas Jefferson National Accelerator Facility, Newport News, Virginia 23606, USA*

(Received 22 June 2021; accepted 21 December 2021; published 3 February 2022)

A concise demonstrative summary of the Symmetric-Hybrid ring design for the storage ring proton electric dipole moment experiment is presented. Critical issues such as lattice design, background electrical fields, geometrical phase, general relativity, spin coherence time, and polarimeter systematics are presented. Overall, we find that with the currently proposed design iteration the systematic error sources are reduced by orders of magnitude and that the ring alignment requirements are within currently available technology.

DOI: 10.1103/PhysRevD.105.032001

I. INTRODUCTION

The latest muon $(g-2)$ results [1–4] have demonstrated the high sensitivity reach of experimental, analytical, and simulation tools with the latter matching and many times surpassing the precision of analytical estimations. Spin and beam dynamics needed to be understood with high precision similar to the level required for a sensitive storage ring electric dipole moment (EDM) experiment. This article describes a high-precision storage ring EDM experiment for the proton as the next generation of high-precision and high-impact physics in storage rings.

The EDM of an elementary particle is proportional to its spin $\vec{S}$, which is odd under time reversal T. Hence, in the presence of an electric field $\vec{E}$, which is invariant under T, the interaction Hamiltonian of the particle $H_{\rm int} \propto -\vec{E}\cdot\vec{S}$ violates T symmetry. This would also imply combined charge conjugation parity (CP) symmetry violation, given CPT conservation, which is encoded in the quantum field theory formulation of the Standard Model (SM).

The weak interactions in the SM mediate well-established CP-violating phenomena and can, through quantum processes, generate nonzero EDMs for constituents of atoms, i.e., electrons and nucleons. However, the electron and nucleon EDMs in the SM are induced at high loop orders and are quite suppressed: $d_e^{\rm SM} \lesssim 10^{-38}\ e\cdot{\rm cm}$ and $d_N^{\rm SM} \lesssim 10^{-32}\ e\cdot{\rm cm}$, respectively; $N=p,\ n$ [5–7]. The EDMs generated by the SM interactions are not observable at current or near-future experiments, making any positive measurement an unambiguous signal of new physics.

It is interesting to note that the SM, in principle, could have generated a large nucleon EDM, through a P-odd and T-odd renormalizeable interaction $\propto \theta G_{\mu\nu}\tilde{G}^{\mu\nu}$, where θ is a fundamental parameter of QCD; $G_{\mu\nu}$ and $\tilde{G}^{\mu\nu}$ denote the field strength tensor and dual tensor of the gluon, respectively. Because of the axial anomaly of QCD, the value of θ gets shifted when quarks are transformed by chiral rotations that diagonalize the quark mass matrix M_q. Thus, the physically observable quantity is given by

$$\bar{\theta} \equiv \theta + \arg[\det(M_q)]. \tag{1}$$

The contribution of $\bar{\theta}$—assuming dominance of the long-range pion loop processes—to nucleon EDMs is estimated to be [5,8–10] ($q=e>0$ is the charge of the proton)

*Corresponding author.
selcuk.haciomeroglu@gmail.com
†Corresponding author.
semertzidisy@gmail.com

$$-d_n(\bar{\theta}) \approx d_p(\bar{\theta}) \approx 10^{-16}\bar{\theta}\ e \cdot \text{cm}. \tag{2}$$

However, the above relation does not in general hold, since there are short-range contributions to $d_n(\bar{\theta})$ and $d_p(\bar{\theta})$ that can in principle have magnitudes similar to that in Eq. (2). There is no reason to expect that the long- and short-range contributions should cancel, and hence one can take the above estimate as a good lower bound [9,10], though a nonperturbative treatment is required for a more definitive result; see, for example, Refs. [10–12]. Given the current bound on the neutron EDM $d_n < 1.8 \times 10^{-26}\ e \cdot \text{cm}$ (90% C.L.) [13], one then obtains $\bar{\theta} \lesssim 10^{-10}$.

Note that $\bar{\theta}$ could be rotated away if one of the quarks is massless, rendering $\arg[\det(M_q)]$ ill defined. That possibility is disfavored by low-energy hadron phenomenology and lattice computations [14–16]. The smallness of $\bar{\theta}$ is therefore a conceptual SM puzzle, since there is no obvious reason why the sum of the contributions in Eq. (1) should cancel so precisely. A well-known resolution of this "strong *CP* problem" is furnished by the Peccei-Quinn (PQ) mechanism [17,18], which provides a dynamical relaxation of $\bar{\theta}$ to zero and gives rise to a light pseudoscalar, the "axion" [19,20]. Nonetheless, contributions from new physics beyond the SM (BSM) can perturb the PQ mechanism and induce a nonzero $\bar{\theta}$ [5].

There are good reasons for assuming BSM phenomena (setting aside gravity which is well described by general relativity). A multitude of observations [21] have established that ∼25% of the cosmic energy budget is made up of an unknown substance—namely, dark matter (DM)—which requires BSM physics (e.g., the PQ axion which can be a good DM candidate). The visible Universe, which accounts for ∼5% of the cosmic total, has a dominance of ordinary matter over antimatter, whose origin is an open fundamental question. In addition, the well-established flavor oscillation of neutrinos calls for nonzero neutrino masses which, again, cannot be accommodated for in the minimal SM. Taken together, one reaches the unavoidable conclusion that BSM physics is required for a more complete description of nature.

Quite generically, BSM theories introduce new interactions with complex couplings and, hence, additional sources of *CP* violation. In fact, an amount of *CP* violation well above the level that the SM provides is a requirement for a successful mechanism to explain the cosmic dominance of matter or, equivalently, the baryon asymmetry of the Universe [22]. Therefore, new *CP*-violating physics and additional contributions to particle EDMs are motivated from a number of key and empirically well-established facts about nature, apart from any conceptual or theoretical arguments.

The SM prediction for a nucleon EDM, while a challenging experimental target, is only about 3 orders of magnitude below the projected reach of a proton storage ring facility, $\sim 10^{-29}\ e \cdot \text{cm}$. Thus, such an experiment has excellent prospects either to find evidence for new physics or else severely constrain it; we will elaborate on this point in the following.

Numerous BSM proposals have been put forth over the last few decades to address the shortcomings of the SM. Many of these ideas have aimed to address the "hierarchy" between the weak scale ∼100 GeV and much larger mass scales, such as the Planck mass $M_{\text{Pl}} \sim 10^{19}$ GeV associated with possible quantum gravity effects. Models based on supersymmetry, weak-scale compositeness, and extra dimensions are some well-known examples. Theories that attempt to explain the hierarchy generally predict the emergence of new physics at energy scales $\lesssim$TeV, providing promising targets for discoveries at the LHC. However, so far, the experiments at the LHC have not yielded any conclusive evidence for BSM physics at $\mathcal{O}(\text{TeV})$ energies.

The above state of affairs has, in part, prompted discussions about future accelerators that can probe well beyond the TeV scale. The enormous cost of such facilities makes it imperative to provide strong physics motivations for their discovery prospects. For example, a pp collider at center-of-mass energy $\sqrt{s} = 100$ TeV, based on current analyses [23], could potentially access new states up to masses $M_{\text{new}} \sim 30$ TeV. While one could speculate about various BSM scenarios that may be discovered at that facility, the detection of a clear proton EDM signal could provide extremely compelling motivation for its construction, as we will briefly discuss below.

Using quark models of hadrons, nucleon EDMs are estimated to be similar in size to quark EDMs and color EDMs, which involve gluons instead of photons. An order-of-magnitude estimate for the one-loop quark EDM is

$$d_q \sim \frac{g^2}{16\pi^2}\frac{e m_q \sin\phi}{M_{\text{new}}^2}, \tag{3}$$

where g is a typical coupling of new physics to a quark with mass $m_q \sim 5$ MeV and ϕ is a BSM *CP*-violating phase. A dipole operator couples left- and right-handed fermions and requires a chiral flip, accounted for by the m_q dependence of the above expression. Let us assume a loop factor $g^2/(16\pi^2) \sim 0.01$, as a typical expectation. We then find

$$d_q \sim 10^{-29}\left(\frac{30\ \text{TeV}}{M_{\text{new}}}\right)^2\left(\frac{\sin\phi}{0.01}\right)\ e \cdot \text{cm}. \tag{4}$$

Thus, under reasonable assumptions, an EDM signal at a proton storage ring experiment can provide a strong physics case for the significant investments required to access scales of $\mathcal{O}(10\ \text{TeV})$ at a future collider. We also point out that $\sin\phi \sim 0.01$ can be considered fairly conservative, given that for the *CP*-violating phase δ in the SM quark sector $\sin\delta \sim 1$ [21]. If we take $\sin\phi \sim 1$ in the BSM sector also, scales up to ∼300 TeV can possibly be probed

TABLE I. Brief description of storage ring designs capable of measuring charged particle EDMs.

Lattice	Comments
Muon $(g-2)$	The tipping angle of the $(g-2)$ precession plane [32] lets us infer the muon EDM value. Limited statistical EDM sensitivity. When electric focusing is used, eventually it will be limited by geometrical alignment, which could require consecutive CW and CCW injections to eliminate it.
E, B fields combined lattice for measuring EDMs of deuteron [33], ^{3}He, proton, etc.	The right combination of E, B fields leads to the "frozen-spin" condition, in principle, at any energy. High statistical sensitivity on EDM. Requires consecutive CW and CCW injection with flipping of the B fields to eliminate the main systematic error source—background vertical electric field (assuming magnetic quadrupoles). Need to demonstrate strict stability of E-field direction with magnetic field flips.
All-electric (4-fold) [34,35]. Electric bending and weak vertical electric focusing.	Requires state-of-the-art magnetic shielding and ability to observe vertical separation of counter-rotating beams at below nano meter level.
Hybrid (4-fold) [36]. Electric bending and alternate (strong) magnetic focusing.	Does not require magnetic shielding due to the effective shielding from radial magnetic fields via magnetic quadrupoles. The lattice is still sensitive to vertical velocity systematic error source (Sec. III A) affecting mainly the DM/DE sensitivity[a] with still significant but manageable impact on EDM measurement.
Symmetric-Hybrid (this work). Same as Hybrid (4-fold) with maximal possible symmetry.	Including the benefits of the Hybrid (4-fold) ring, this design effectively eliminates the largest systematic error source—vertical velocity (Sec. III A), impacting mostly the DM/DE sensitivity. It also makes the EDM experiment easier by reducing this potentially large systematic error source.

[a]DM/DE sensitivity refers to vertical spin build-up due to unavoidable radial spin component (see Sec. III A), and DM/DE and EDM separation is discussed in Ref. [37]. Importantly, a finite EDM is not a necessary condition for the DM/DE experiment and vice versa.

through the proton EDM measurement, well beyond the reach of any collider envisioned for the foreseeable future.

The recent years have seen a surge of interest in new ideas for BSM particles at or below the GeV scale that have suppressed coupling to the SM; see, for example, Refs. [24,25]. Such physics may originate from a "dark sector" that includes DM and only indirectly interacts with the visible world. Also, given the apparent absence of BSM states near the TeV scale, it is worth considering that new physics could have a low-energy scale but require intense sources to access, due to its feeble interactions with the SM. Adopting this point of view, one may consider $M_{\rm new} \sim 1$ GeV in Eq. (3), which yields a proton storage ring sensitivity to $g \lesssim 3 \times 10^{-5}$. This greatly exceeds current and projected sensitivity for the coupling of new light states to quarks, under various assumptions for BSM physics; see, for example, Refs. [26–28].

Finally, we note that the first results of the experiment E989 at Fermilab that were released recently [1] confirm the long-standing muon $(g-2)$ measurements at Brookhaven National Laboratory [29]. The combined results point to a 4.2σ deviation from the SM theory prediction of Ref. [30] (however, see also Ref. [31]). If this deviation persists with more data and further scrutiny of the SM theory, it would be a harbinger of new physics. That physics could potentially also manifest itself via a proton EDM measurement. In that case, the complementary precision signals from the lepton and hadron sectors could provide valuable insights about the nature of the underlying BSM phenomena and help chart a course for a new era of discovery.

The storage ring proton EDM method targets $d_p = 10^{-29}\ e \cdot \mathrm{cm}$, which is more than 3 orders of magnitude better than the current best neutron EDM limits [13]. We also claim that this sensitivity is achievable with existing technology thanks to the significantly relaxed alignment requirements with the Symmetric-Hybrid ring design.

There are multiple ways to design a lattice capable of measuring a charged particle EDM, some of which are described in Table I. Although there are a number of choices, the one with the least systematic error sources (potential risk) is chosen here for a comprehensive study—Symmetric-Hybrid design.

Although the direct measurement of charged particle EDM is challenging, the Muon $(g-2)$ experiments using storage rings have been setting the best direct EDM limits on muons. Similar to $(g-2)$, the proton EDM also uses the so-called magic momentum; though the muon $(g-2)$ experiment at Fermilab uses magnetic bending and electric focusing to study the muon magnetic anomaly with high precision, the proton EDM proposal is to use electric bending and alternate magnetic focusing as the best way to reduce systematic error sources. No magnetic bending leads to lock-in of the average spin directions with the momentum, which is also recognized as "frozen" spin (more in Sec. II A). A nonzero EDM causes a linear vertical spin build-up that is measured as a function of beam storage time to infer the EDM value.

The most prominent systematic error source in the storage ring designs based on the All-electric ring [34] is the background radial magnetic field—B_x^{external}. The stray magnetic field is the most challenging requirement [36]. To overcome such a shielding requirement, the next iteration after the All-electric ring, the Hybrid (4-fold) ring design [38] was developed. It has been a major accomplishment since any B_x^{external} is naturally shielded by the magnetic focusing system. The Hybrid (4-fold) ring design features a strong alternating magnetic focusing with electric bending that still allows simultaneous clockwise (CW) and counterclockwise (CCW) beam storage. Counter-rotating (CR) beams are crucial to avoid the first-order systematic error source—a vertical dipole E field.

In rings where the main vertical focusing is magnetic [e.g., Hybrid (4-fold)], the main systematic error source becomes the out-of-plane (vertical) electric field. However, this systematic error cancels exactly for vertical dipole electric fields with CR beams. It is the only lattice that accomplishes this cancellation, and as such, it represents a major breakthrough in the storage ring EDM field. The next-level systematic error source is the fact that the average vertical velocity integrated over electric field sections might not be zero. This is a strict requirement for the case of radial polarization, able to probe dark matter and dark energy (DM/DE) [37] and has been relaxed by several orders of magnitude by making the lattice highly symmetric.

In this work, the newest design iteration, the Symmetric-Hybrid ring, relaxes requirements established by the Hybrid (4-fold) ring by several orders of magnitude, provides comprehensive systematic error analysis, and standardizes experimental techniques. Highlighted novelties of this work include:

(i) Symmetric-Hybrid lattice design (Secs. II A and III C),
(ii) spin-based alignment (Sec. III C),
(iii) hybrid sextupole configuration for simultaneous spin coherence time (SCT) improvement for CR beams (Sec. III F).

By providing solutions to the most significant systematic error sources and designing a storage ring with realistic specifications, this work aims to be the foundational basis for the storage ring proton EDM experiment.

The rest of the paper is structured as follows. Section II provides an introduction to the experimental technique and the tools used in this work. Section III discusses the major systematic error sources. Section IV concludes the work by providing the relevant discussions.

II. METHODS

A. Experimental technique

The spin $\vec{S}$ precession rate for a particle at rest in the presence of magnetic $\vec{B}$ and electric $\vec{E}$ fields is given as

$$\frac{d\vec{S}}{dt} = \vec{\mu} \times \vec{B} + \vec{d} \times \vec{E},$$

where magnetic and electric dipole moments are defined as $\vec{\mu} = (gq/2m)\vec{S}$ and $\vec{d} = (\eta q/2mc)\vec{S}$, respectively.

Spin motion relative to the momentum for a particle with $\vec{\beta} = \vec{v}/c$ in a cylindrical coordinate system[1] is given as [39–41]

$$\vec{\omega}_a = -\frac{q}{m}\left(G\vec{B} - \frac{G\gamma}{\gamma+1}\vec{\beta}(\vec{\beta}\cdot\vec{B}) - \left(G - \frac{1}{\gamma^2-1}\right)\frac{\vec{\beta}\times\vec{E}}{c} + \frac{1}{\gamma}\left[\vec{B}_{\parallel} - \frac{1}{c\beta^2}(\vec{\beta}\times\vec{E})_{\parallel}\right]\right)$$

$$\vec{\omega}_\eta = -\frac{\eta q}{2m}\left(\frac{\vec{E}}{c} - \frac{\gamma}{\gamma+1}\frac{\vec{\beta}}{c}(\vec{\beta}\cdot\vec{E}) + \vec{\beta}\times\vec{B}\right),$$

where ω_a and ω_η stand for precession due to magnetic and electric dipole moments, respectively, and G stands for the proton magnetic anomaly. For $\vec{\beta}\cdot\vec{E} = 0$ and $\vec{\beta}\cdot\vec{B} = 0$, the motion of the spin vector simplifies more,

$$\vec{\omega}_a = -\frac{q}{m}\left(G\vec{B} - \left(G - \frac{1}{\gamma^2-1}\right)\frac{\vec{\beta}\times\vec{E}}{c} + \frac{1}{\gamma}\left[\vec{B}_{\parallel} - \frac{1}{c\beta^2}(\vec{\beta}\times\vec{E})_{\parallel}\right]\right) \tag{5}$$

$$\vec{\omega}_\eta = -\frac{\eta q}{2m}\left(\frac{\vec{E}}{c} + \vec{\beta}\times\vec{B}\right)$$

$$\vec{\Omega} = \vec{\omega}_a + \vec{\omega}_\eta$$

$$\frac{d\vec{S}}{dt} = \vec{\Omega}\times\vec{S}, \tag{6}$$

with $\parallel$ indicating horizontal (in-plane) projection of a vector.

We set $\vec{B} = 0$[2] and choose "magic momentum" such that $\gamma = \sqrt{1 + 1/G}$. For protons, the "magic" parameters are given in Table II. By choosing such proton momentum, Eq. (5) leads to

$$\vec{\omega}_a = \frac{q}{m\gamma c\beta^2}(\vec{\beta}\times\vec{E})_{\parallel}. \tag{7}$$

Notably, a vertical electric field would create a nonzero radial component for $\vec{\omega}_a$, which would look like the EDM

[1] i.e., in standard right-handed accelerator Frenet-Serret x, y, s coordinates. This coordinate system is used throughout the work unless stated otherwise.

[2] Setting $\vec{B} = 0$ is not technically correct due to having magnetic quadrupoles, but it is helpful to assume temporarily.

TABLE II. Magic parameters for protons, values obtained from Ref. [44].

G	β	γ	p	KE
1.793	0.598	1.248	0.7 GeV/c	233 MeV

signal with one beam direction. With horizontal $\vec{E}$ fields and $\vec{\beta}$ ($\vec{E} = \vec{E}_{\parallel}, \vec{\beta} = \vec{\beta}_{\parallel}$), the equation simplifies further into $\vec{\omega}_a = 0$, which is also known as the frozen spin condition. In this arrangement, the spin precesses into the vertical direction only due to the EDM contribution,

$$\Omega \propto \eta E,$$

linearly in the timescale of the injection $\Omega \propto dS_y/dt$. $dS_y/dt \propto E\eta$ is the fundamental principle of measuring the proton EDM. That is, measurement of the out-of-plane spin precession rate (dS_y/dt) inside a storage ring probes the intrinsic EDM of the particles. The coupling of the electromagnetic fields to a particle's magnetic dipole moment is orders of magnitude larger than the EDM coupling. Hence, a strict alignment requirement of electromagnetic fields is necessary. Further details about the storage ring EDM experiment could be found in Refs. [42,43].

The Symmetric-Hybrid ring design used in this study consists of 24 FODO (focusing-drift-defocusing-drift accelerator structure) sections making up 800m in longitudinal length. Each FODO section comprises a pair of electric bending sections (more about electric fields and electrode design is in Appendix A) and a pair of magnetic quadrupoles. An illustration of a single FODO is given in Fig. 1. A schematic of the ring is given in Fig. 2. Dispersion and beta functions are given in Fig. 3, and the slip factor is given in Fig. 4.

The design leaves 4.16 m of straight sections between electrostatic bends. The straight sections are chosen to be sufficiently long for a vertical injection of CR beams, polarimeters, radio frequency (RF) cavities, and other apparatus. Notably, straight sections could be made longer at the cost of increasing the electric field strength in the bending sections, i.e., by changing the ratio of circular/bending lengths while retaining the total length of the lattice. The injected beam momentum is quite soft, and an injection scheme has been worked out assuming only presently standard technology. The CR beams will be

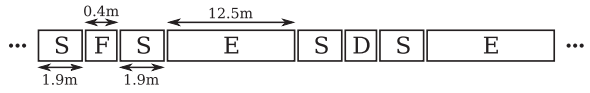

FIG. 1. Schematic view of a single FODO cell. The entire ring is composed by stacking this unit 24 times. Legend: F: focusing quadrupole; D: defocusing quadrupole; S: straight free drift; E: electric bending.

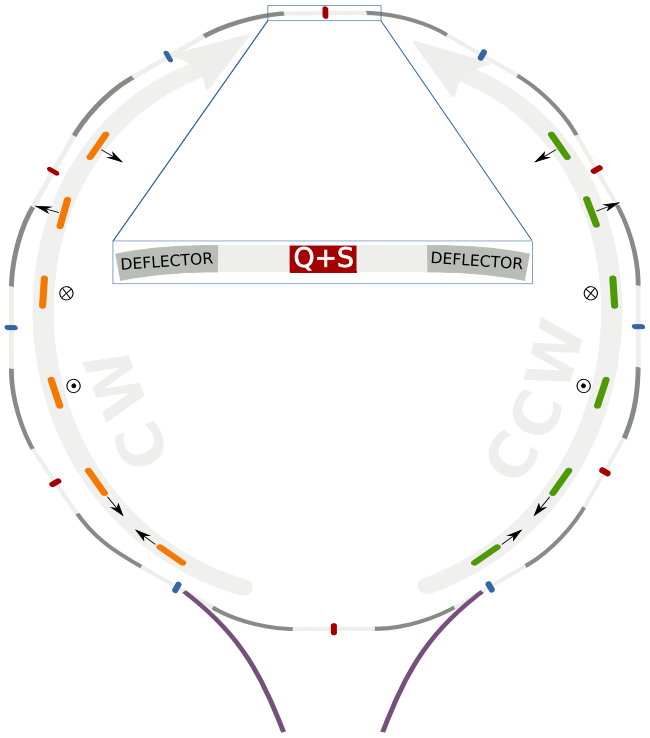

FIG. 2. Schematic top view of the Symmetric-Hybrid ring. Both CR beams have longitudinally, radially, and vertically polarized bunches with different helicities (arrows in dark color). Blue and red correspond to focusing and defocusing quads. Naturally, CR beams see the opposite focusing effect from magnetic quads. The actual number of FODO sections is 24.

injected one after the other with their polarization in the vertical direction. The beam will then be let to debunch, with an RF cavity rebunching both CR beams with parameters as shown on Table III. Subsequently, a standard RF solenoid will be used to create bunches with longitudinal polarizations (both helicities) and radially polarized bunches pointing inward/outward of the ring center.

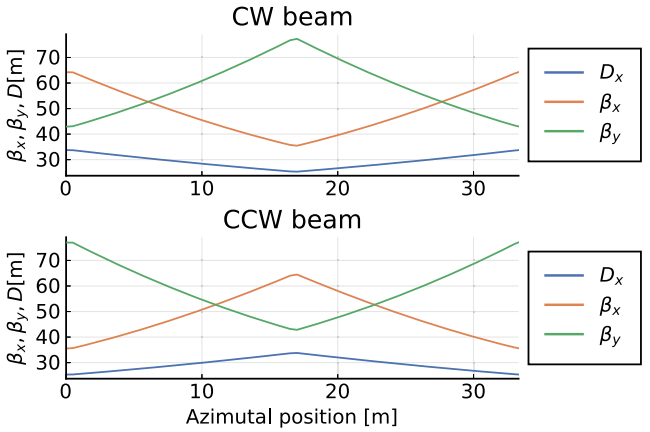

FIG. 3. Superperiod structure, beta functions, and dispersion (the β letter within text of the paper always refers to velocity).

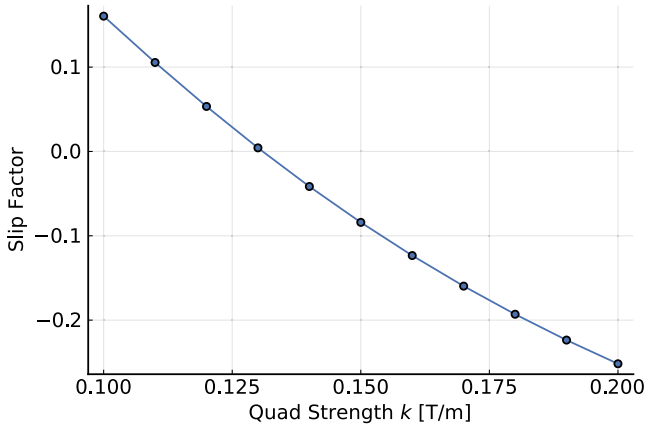

FIG. 4. The slip factor is obtained from evaluating $\frac{dt}{t}/\frac{dp}{p}$ per turn via numerical tracking. A negative slip factor corresponds to below transition operation, which is essential with the intrabeam scattering considerations.

As the estimations have shown, the slip factor (Fig. 4) needs to be negative in order for the intrabeam scattering (IBS) not to cause severe beam lifetime issues. With beam storage times of $\approx 10^3$ sec $= 17$ min in mind, IBS becomes the primary mechanism of the emittance growth and consequently of particle loss. For the current ring design, the beam lifetime is estimated to be 22 min due to IBS and residual gas scattering assuming the vacuum level 10^{-10} torr of atomic hydrogen equivalent. The beam will be lost primarily on the polarimeter target due to IBS-induced exchange of horizontal and vertical emittance. The betatron tunes are optimized to avoid resonances up to eighth order inclusively, with the consideration of space charge and beam-beam tune shifts. The selected tunes were confirmed to be free of beam resonances with simulation. Additionally, the lattice is compatible with stochastic cooling, which might be used to further prolong the spin coherence time (Sec. III F) and the beam lifetime.

More specifications and details are given on Table III.

TABLE III. Ring and beam parameters for the Symmetric-Hybrid ring design.

Quantity	Value
Bending radius R_0	95.49 m
Number of periods	24
Electrode spacing	4 cm
Electrode height	20 cm
Deflector shape	Cylindrical
Radial bending E field	4.4 MV/m
Straight section length	4.16 m
Quadrupole length	0.4 m
Quadrupole strength	± 0.21 T/m
Bending section length	12.5 m
Bending section circumference	600 m
Total circumference	800 m
Cyclotron frequency	224 kHz
Revolution time	4.46 μs
$\beta_x^{\max}, \beta_y^{\max}$	64.54 m, 77.39 m
Dispersion, $D_x^{\max}$	33.81 m
Tunes, Q_x, Q_y	2.699, 2.245
Slip factor, $\frac{dt}{t}/\frac{dp}{p}$	-0.253
Momentum acceptance, (dp/p)	5.2×10^{-4}
Horizontal acceptance (mm · mrad)	4.8
RMS emittance (mm · mrad), ϵ_x, ϵ_y	0.214, 0.250
RMS momentum spread	1.177×10^{-4}
Particles per bunch	1.17×10^8
RF voltage	1.89 kV
Harmonic number, h	80
Synchrotron tune, Q_s	3.81×10^{-3}
Bucket height, $\Delta p/p_{\text{bucket}}$	3.77×10^{-4}
Bucket length	10 m
RMS bunch length, σ_s	0.994 m

B. High-precision tracking

A Runge-Kutta family integrator (fifth order, adaptive step size [45]) was used in order to perform simulations throughout this work. It was cross-checked by at least one independent effort for most of the shown studies. Both beam and spin dynamics are fully tracked numerically. Particle beam dynamics are treated with perturbative expansion of the Lorentz equation around the reference orbit in a Frenet-Serret coordinate system, with the spin tracked via the Thomas-Bargmann-Michel-Telegdi (T-BMT) equation. More details are given in Appendix D.

III. SYSTEMATIC ERROR SOURCES

The primary quantity of interest is the vertical spin precession rate dS_y/dt that lets us estimate the intrinsic dipole moment of the proton d_p. The target sensitivity of $d_p = 10^{-29}$ $e \cdot$ cm corresponds to a vertical spin precession rate of $dS_y/dt = 1$ nrad/s (this number will be useful throughout the work). Thus, any non-EDM originating vertical spin precession rate larger than 1 nrad/s is considered a potential systematic error source.

Ideally, the EDM search is accomplished with positive helicity CR 100% longitudinally polarized beams. Realistically, as little as a $\approx 10^{-3}$ rad average radial spin component would be uncontrollable due to statistical limitations alone (see Sec. III G). Some systematics (e.g., vertical velocity; see Sec. III A) are only sensitive to the radial spin component—S_x. Such systematics must always be considered not only due to little average radial spin component being present (inadvertently) but also due to free horizontal spin precession oscillations due to lattice imperfections.

The initial average spin direction, between maximally longitudinal and maximally radial polarization directions, could be controlled—the initial S_s/S_x ratio. Choosing this ratio is a powerful tool to clearly differentiate the systematic error sources into longitudinal and radial polarization originating types.

TABLE IV. Summary of the main systematic error sources in storage ring EDM rings. "T-BMT term" indicates the driving term in Eq. (5) which lets us infer the sensitive polarization direction.

Name	T-BMT term	Comments
Radial magnetic field	$S_s \cdot B_x$	Main systematic error source in the All-electric ring design but not in rings with magnetic focusing. In rings with strong magnetic focusing [Hybrid (4-fold) and Symmetric-Hybrid], the external magnetic field is completely shielded out. Find more details in Ref. [38].
Vertical electric field (dipole)	$S_s \cdot \beta_s \cdot E_y$	Incorporation of CR beams completely eliminates this effect, as the vertical spin precession created by the vertical electric field is in the direction opposite of the true EDM signal. This is expected to be the largest systematic error source for rings without simultaneously stored CR beams. Trim vertical-electric-field plates, symmetrically distributed around the ring, will be used to keep the same sign vertical spin precession rate to zero for the CR beams.
Vertical velocity	$S_x \cdot \beta_y \cdot E_x$	Main systematic error source for DM/DE in Hybrid (4-fold) ring design and of a secondary concern for the EDM target sensitivity. By making the lattice symmetric—Symmetric-Hybrid lattice (this work)—this effect reduces by several orders of magnitude, making it acceptable for the DM/DE target and completely negligible for the EDM sensitivity. More discussion is found in Sec. III A.
Vertical electric field (quadrupole)	$S_s \cdot \beta_s \cdot E_y$	All effects that depend on the CR beams separation, either in the vertical or in the horizontal direction, can be easily eliminated by artificially enlarging the separation with the application of small dipole magnetic fields at the magnetic quadrupole locations. By selectively splitting the CR beams using dipole correctors of the magnetic quadrupoles, the value of the parasitic electric (skew) quadrupole can be measured precisely and corrected. More details is found in Sec. III C.

In the following subsections, relevant to the EDM search, potential systematic error sources will be discussed. With the mentioned mixing of polarizations in mind, the systematics pertaining to the radial polarization direction has its effect reduced for the EDM search (longitudinal polarization) by at least a factor of 10^3. The horizontal spin precession rate of the CR beams will be controlled using feedback with a combination of machine (RF-cavity) frequency and vertical magnetic trim fields. A brief summary of the systematic error sources is given in Table IV.

A. Vertical velocity

The vertical velocity systematic error originates from the term proportional to

$$(\vec{S} \times (\vec{\beta} \times \vec{E})_s)_y = S_x \cdot \beta_y \cdot E_x \tag{8}$$

in the spin dynamics equation—Eqs. (6) and (7). Nonzero radial spin component S_x (pointing outward from the ring center) combined with vertical velocity β_y may create vertical spin precession that would be indistinguishable from EDM even with CR beam injection.[3]

Despite $\langle \beta_y \rangle \equiv 0$, the velocity would be nonzero if averaged over the bending sections only (E_x field regions). Formally, we can only expect

$$L_{\text{straight}} \langle \beta_y \rangle_{\text{straight}} + L_{\text{bending}} \langle \beta_y \rangle_{\text{bending}} = 0;$$

each of the $\langle \beta_y \rangle_{\text{straight}}$ and $\langle \beta_y \rangle_{\text{bending}}$ might not be zero individually. This leads to a possibility of

$$\langle \beta_y \cdot E_x \rangle \neq 0,$$

and

$$dS_y/dt \propto \langle S_x \cdot \beta_y \cdot E_x \rangle \neq 0,$$

which is the essence of the effect.

This systematic is also known as vertical orbit corrugation or the "rollercoaster effect." It is most prominent in the radial polarization case; thus, its effect is at least a few orders of magnitude less in longitudinal (applicable to the EDM search) polarization. To isolate and understand this effect better, we put the beam in radial polarization and create vertical orbit corrugation by vertically misaligning one magnetic quadrupole at a time. A single vertically misaligned quad induces vertical imbalance that creates a nonzero average vertical velocity.

The vertical velocity systematic is especially prominent in ring designs where all the quadrupoles are not equivalent in misalignments with respect to each other. For example, the Hybrid (4-fold) ring design [38] (Fig. 5), where misaligned quads are not equivalent (symmetric), shows clear islands of tolerance to vertical quad misalignments, Fig. 6(a). Only the quads at locations where the ring looks the same in both directions longitudinally, the Hybrid

[3]Subscript s indicates the direction along the ring azimuth.

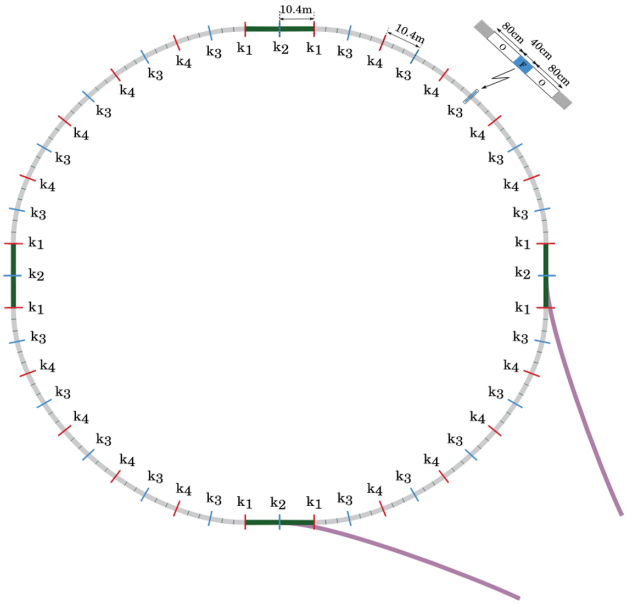

FIG. 5. Hybrid (4-fold) ring design; the presence of the long straight sections severely reduces the number of symmetric points in azimuth (adapted from Ref. [34]).

(4-fold) ring, are insensitive to the corresponding misalignments [dips in Fig. 6(a)].

By making the ring symmetric for all the quads longitudinally (Fig. 2), all the quadrupoles are made equivalent and thus tolerant to vertical misalignments—Fig. 6(b). The quadrupoles were misaligned one at a time by 100 μm, which splits the CR beams by around 250 μm. Vast reduction of the background vertical precession rate is achieved [Fig. 6(b)] with the Symmetric-Hybrid ring design, therefore reducing the systematic error source by a few orders of magnitude.

Distributing the quadrupole misalignments randomly with rms $\sigma = 100$ μm that leads more than 1 mm CR beam separation has been tested, too. Background vertical spin precession with radially polarized beam does not exceed 1 nrad/s in the Symmetric-Hybrid lattice.

B. Dipole *E* field

The dipole E-field systematic originates from the

$$(\vec{S} \times (\vec{\beta} \times \vec{E})_x)_y = S_s \cdot \beta_s \cdot E_y$$

term in Eqs. (6) and (7). A nonzero E_y could arise due to some tilt ($x - y$ plane rotation) in the deflector plates. Each bending section, being randomly tilted, contributes to the average nonzero dipole E field initially present in the storage ring. E_y creates an EDM-like signal for one of the counter-rotating beams. However, the true EDM-signal causes a vertical spin precession in opposite directions for CR beams. The difference of precession rates for CR beams gives us the true EDM signal, as the dipole E field creates a

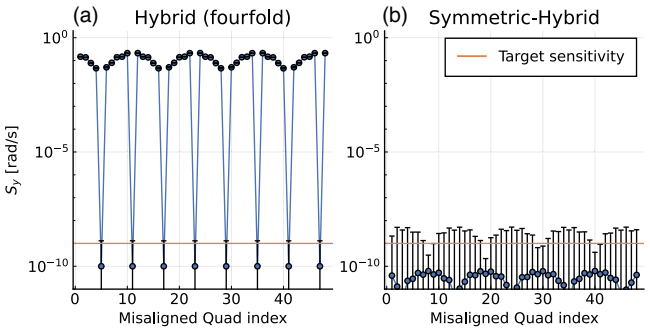

FIG. 6. *Radial polarization case* $S_x = 1$, sensitive to DM/DE (even though the vertical velocity effect directly only affects the DM/DE sensitivity, if it is too large, it will inevitably affect the EDM sensitivity of the stored bunches with primarily longitudinal polarization as well). Vertical spin precession rate vs index of the 100 μm vertically misaligned quad (one at a time) along the azimuth. The orange lines correspond to the target EDM sensitivity. (a) The original Hybrid (4-fold) ring design is used (Fig. 5). Dips of the graph correspond to quads in the center of the four long straight sections (in green color) shown in Fig. 5 and the quads maximally away from long straight sections. (b) The Symmetric-Hybrid ring design is used (Fig. 2). Notably, the performance is many orders of magnitude better than the Hybrid (4-fold) ring (a). Simulations with lattice parameters slightly off their ideal values do not seem to show a significant deterioration of the cancellation factor. Some of the error bars extend beyond zero which makes them partially invisible in the log-scale plot. Such large error bars hint that the true underlying precession rate is zero with large oscillations. Error bars arise due to an inability to determine the exact vertical precession rate from finite digital data (numerical tracking). There is more about this in Appendix B.

discernible from EDM signal with CR beam storage—Fig. 7 ($N = 0$). Formally,

$$\left(\frac{dS_y}{dt}\right)_{\text{EDM}} = \frac{1}{2}\left(\frac{dS_y}{dt}\right)_{\text{CW}} - \frac{1}{2}\left(\frac{dS_y}{dt}\right)_{\text{CCW}}.$$

More about spin data combinations is given in Appendix C.

An average background E_y—Fig. 7 ($N = 0$)—creates a large spin precession in both CR beams. Such a large spin precession, but the same for CW and CCW beams, is undesirable for a multitude of reasons. In practice, a trimming E_y^{trim} dipole electric field will be applied to compensate for the large spin precession such that no discernible spin precession ($<10^{-6}$ rad/s) is seen in both CR beams that effectively sets $E_y + E_y^{\text{trim}} = 0$. Gradual adjustment of E_y^{trim} will eliminate same direction (non-EDM like) vertical spin precession in both CR beams.

C. Quadrupole *E*-field and spin-based alignment

In the absence of vertical electric fields $E_y^{\text{external}} = 0$, any nonzero B_x^{external} would be compensated by a magnetic force coming from quadrupoles; therefore, it would on

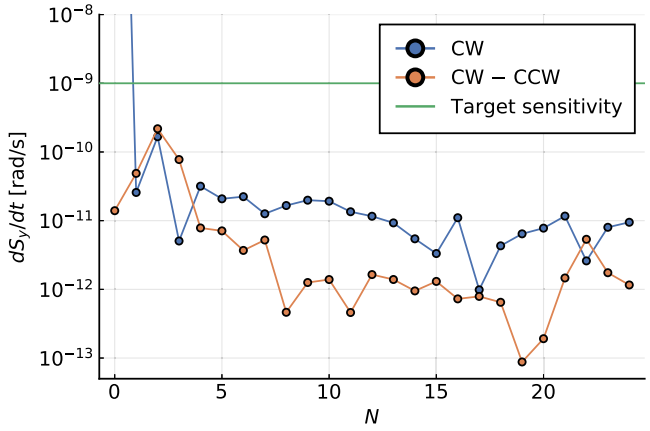

FIG. 7. *Longitudinal polarization case* $S_s = 1$, sensitive to EDM. Vertical spin precession rate vs $E_y = 10$ V/m field N harmonic around the ring azimuth. For $N = 0$, the precession rate for the CW (or CCW) beam is around 5 rad/s. The difference of the precession rates for CR beams (orange) is below the target sensitivity for all N. Irregularities of the low values are due to the inability to determine the exact precession rate from the simulation results. Hence, the points only show a statistical upper limit of the possible vertical precession rate; actual rates could be lower. More about this is in Appendix B.

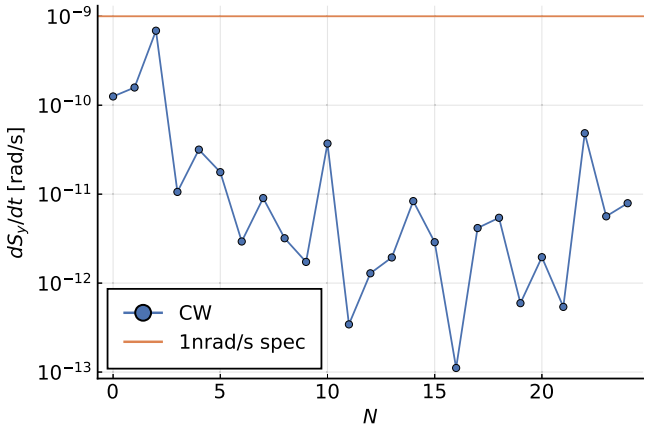

FIG. 8. *Longitudinal polarization case* $S_s = 1$, *CW beam only.* Vertical spin precession rate vs $B_x = 1$ nT field N harmonic around the ring azimuth. The magnetic field amplitude is chosen to be similar to beam separation requirements in Sec. IV A, and more than $B_x = 1$ nT splits the CR beams too much. Irregularities of the low values are due to the inability to determine the exact precession rate from the simulation results. Hence, the points only show a statistical upper limit of the possible vertical precession rate; actual rates could be lower. More about this is in Appendix B.

average result in $\langle B_x \rangle = 0$. Magnetic fields are balanced by magnetic fields; hence, there is no apparent vertical spin precession due to B_x^{external} for all the $N = 1, 2, 3, \ldots, 24$ harmonics—Fig. 8.

However, in case $E_y^{\text{external}} \neq 0$, $\langle B_x \rangle = 0$ is no longer guaranteed. We can only expect to first order, omitting "external" superscript,[4]

$$F_y = q(E_y + c\beta_s B_x) = 0. \tag{9}$$

Equation (9) needs to be true on average for the closed orbit. But zero on average does not guarantee local absence of electric and magnetic forces. To prevent parasitic vertical spin precession due to E_y^{quad} and B_x, all the multipoles and harmonics need to be addressed individually.

The most dominant multipole, the dipole (E_y), and all its harmonics do not create EDM-like signal due to the simultaneous CR beam storage (Fig. 7). This is also true for higher odd multipoles—i.e., sextupole, decapole, 14-pole, etc.

The quadrupole (E_y^{quad}) and higher-order even multipoles, i.e., octupole, 12-pole, etc., need to be addressed separately. If CR beams are on average separated by $\pm\Delta y$ due to external B_y field in presence of parasitic quadrupole $E_y^{\text{quad}} = K_e \Delta y$, the vertically separated beams would experience electric field in opposite directions $E_y^{\text{quad}} = \pm K_e \Delta y$; therefore, an EDM-like vertical spin precession is observed.

Whenever an electric field balances a magnetic field and vice versa, a vertical spin precession might take place. The All-electric ring design is completely immune to stray electric fields but highly sensitive to radial magnetic fields. The Hybrid (4-fold) and Symmetric-Hybrid designs, in contrast, are sensitive to electric fields. However, the effect of the main multipole—dipole E_y field—is distinguishable from the true EDM signal with CR beam storage.

The presence of E^{quad} can be monitored by controlling B_x.[5] The combination of E^{quad} and B_x produces nonzero vertical spin precession rate dS_y/dt. B_x could be made large on purpose, for example, by controlling dipole correctors of the magnetic quadrupoles. Being able to freely control B_x and all of its harmonics[6] lets us selectively (for each N harmonic) amplify and then reduce the effect of initially unknown E^{quad}.

Likewise, skew electric quadrupoles $E_y^{\text{skew q.}}(x) = K_{e'} x$ couple to vertical magnetic field B_y to create false EDM signals. Measurement of $E^{\text{skew q.}}$ is performed with the same procedure. By purposely introducing B_y using the dipole correctors of the magnetic quadrupoles, measurement of $dS_y/dt \propto E^{\text{skew q.}} \times B_y$ lets us infer the value of $E^{\text{skew q.}}$ for all relevant N values.

Similarly, image charge, beam-beam, etc., effects that may produce quadrupole or higher electric field multipoles are treated the same way. We do this since the effect on the

[4] β_s can safely be assumed constant, as its variation is negligibly small.

[5] More about measuring B_x is in Sec. IV B.

[6] Because of the low tune (≈2), only a few harmonics need to be probed.

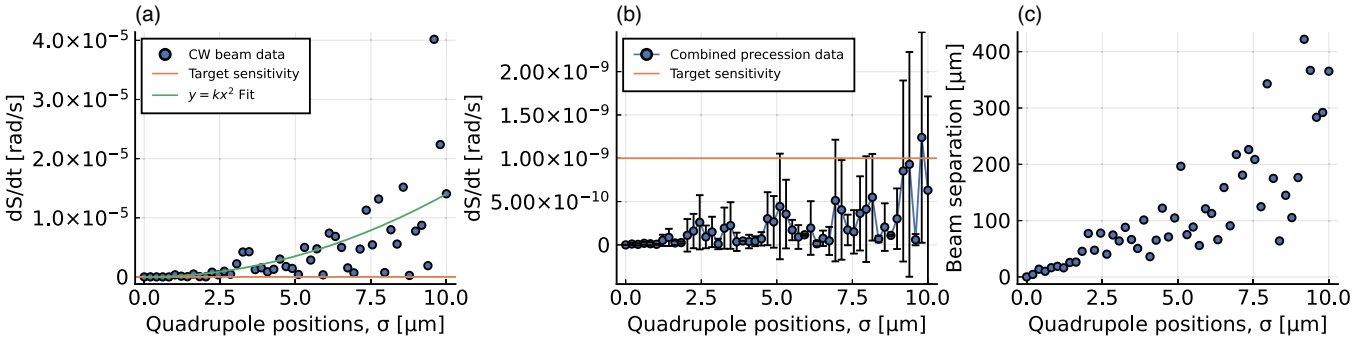

FIG. 9. (a) *Longitudinal polarization case, CW beam only.* Vertical spin precession rate (absolute) vs random misalignments of quadrupoles in both x, y directions by rms σ with different seeds per each point (when the same seeds are used everywhere, the $y = kx^2$ fit is perfect, meaning that every point can be extrapolated to any rms σ value using this functional form). Combination with CCW and quadrupole polarity switching achieves large cancellation—see part (b). (b) *CW and CCW beam and with quadrupole polarity switching.* Total combination as presented in Appendix C. Notably, the background vertical spin precession rate (absolute) stays below the target sensitivity. Irregularity of the points is discussed in Appendix B. (c) Correspondence between CR beam separation and rms σ quadrupole misalignments.

vertical spin precession rate does not depend on the origin of the electric field.

The presented idea of controlling the E fields using spin measurements, which are extremely sensitive, is labeled as "spin-based alignment" (SBA). Leveling the ring to a high order using SBA is performed using various combinations of the bunch polarizations. For example, radial polarization bunches, being sensitive to vertical velocity (Sec. III A), will be used as a feedback to measure the vertical orbit corrugation. Other spin polarization directions such as vertical polarization can be used to test the effects of geometrical phase and other as yet unknown systematics.

In principle, SBA could be used in other accelerator facilities that require precise ring alignment. The spin dynamics is much more sensitive to electro-magnetic (EM) fields than the beam dynamics; thus, it can serve as a sensitive probe of lattice imperfections.

D. Geometrical phase

The geometrical (Berry) phase effect, as it is known in its most common definition [46–48], is attributed to an extra acquired phase difference when a given system undergoes a cyclic adiabatic process.

In the context of storage ring EDM experiments, unwanted spin precession, obtained due to noncommutativity of successive rotations, is referred to as the geometrical phase. The spin precession is proportional to the product of successive rotation amplitudes.

The product dependence is verified by linearly increasing the amplitude of successive rotations in the x, y plane. This is accomplished by misaligning all magnetic quadrupoles randomly with rms σ (both x, y directions). By increasing σ while observing the growth of the unwanted vertical precession rate, the square dependence is favored—Fig. 9(a). Significant cancellation is achieved by incorporating both CR beams [49] including runs with reversed magnetic quadrupole polarities—Fig. 9(b). As it is apparent from Fig. 9(c), even small quadrupole magnet misalignment causes large CR beam splitting, which will be finely reduced to well below 100 μm by applying dipole correction B fields at the quad locations.

Since the quads are misaligned randomly, it is not immediately clear what is causing the total effect. A thorough study using a straight lattice[7] was performed to reveal that random misalignments of quads alone do not cause vertical spin build-up. Hence, we conclude that the vertical spin precession in one direction [CW—Fig. 9(a)], arises due to intermixing with other systematic effects such as vertical velocity and other second-order systematics (some are discussed in Appendix E).

Numerical tracking shows that the EDM-like vertical spin precession caused due to the geometrical phase is insignificant when the CR beam separation is below a few hundred micrometers (corresponding to quadrupole misalignments of around few micrometers)—Figs. 9(b) and 9(c)—while orbit planarity even around 10 μm was achieved [50,51] by mechanical means using water levels. More about beam separation measurements appears in Sec. IV B.

E. General relativity

General relativistic (GR) effects caused by gravity and rotation of the Earth can be observed in high-precision experiments. The spin dynamics in the considered proton EDM (pEDM) experiment could be affected. In connection with the Equivalence Principle, one can always introduce a *local* Lorentz (anholonomic) coordinate system based on a tetrad of appropriate orthogonal coordinate vectors. Dynamics of the momentum and spin in this coordinate

[7]A straight lattice stripped of electrostatic bends, consisting of only quadrupoles. It is essentially of infinite length that repeats itself every 800 m (including the misalignments).

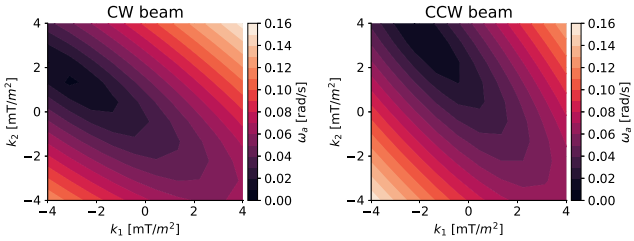

FIG. 10. Single-particle horizontal precession rate ω_a as a function of magnetic sextupole strengths k_1, k_2. Darker: lower ω_a, thus a better SCT. Left: CW beam; right: CCW beam. The axis of the symmetry is $k_1 = -k_2$, hence the apparent transposition with respect to CR beams.

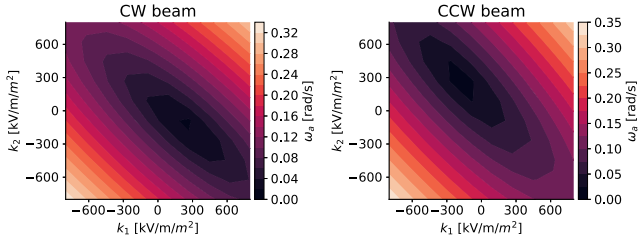

FIG. 11. Single-particle horizontal precession rate ω_a as a function of electric sextupole strengths k_1, k_2. Darker: lower ω_a, thus a better SCT. Left: CW beam; right: CCW beam. The axis of the symmetry is $k_1 = +k_2$, hence the apparent transposition with respect to CR beams.

system is defined by equations of motion formally being the same with the usual equations given by electrodynamics in the Minkowski spacetime [52–54]. The general relativistic effects in storage ring EDM experiments have been analyzed in previous studies [54–58], and the corresponding systematic corrections have been calculated. It has been explicitly shown in Ref. [58] that the final results obtained in these studies perfectly agree with each other. The net effect due to GR creates a little or a distinguishable-from-the-EDM signal with CR beam storage. Hence, GR related effects are not significant for the current proposal.

F. Spin coherence time

The SCT, also known as in plane polarization lifetime, is essential to achieve the desired sensitivity requirements [42]. An EDM search with a longitudinally polarized beam requires a SCT of around 10^3 s. It has been shown that long SCTs are correlated with zero chromaticity conditions [59,60]. Chromaticity is defined as

$$\xi_{x,y} = \frac{\delta Q_{x,y}/Q_{x,y}}{\delta p/p}.$$

Sextupoles can reduce chromaticity and hence make it possible to achieve a long $\approx 10^3$ s SCT, as has been experimentally shown at cooler synchrotron (COSY) [61]. However, our studies show that in a ring with electric bending, as opposed to rings with regular magnetic bending, the required conditions are not exactly the same. Therefore, we focused on directly searching for a long SCT.

A long SCT could be achieved by using magnetic sextupoles. Magnetic sextupole fields are defined as

$$B_x = 2k^m xy$$
$$B_y = k^m(x^2 - y^2).$$

A magnetic sextupole pair k_1^m, k_2^m overlaps with the magnetic quadrupoles (Fig. 1) in order not to break the symmetry requirements of the lattice. The reference particle horizontal precession rate is significantly improved if the correct sextupole fields are used—Fig. 10.

The sextupoles could also be electric instead,

$$E_y = -2k^e xy$$
$$E_x = k^e(x^2 - y^2).$$

A similar spin precession behavior is seen—Fig. 11.

However, the optimal pair (electric or magnetic) of sextupole strengths $k_1^{m,e}, k_2^{m,e}$ (Figs. 10 and 11) is not symmetric with respect to CR beams. It first seems that the SCT can be improved for one beam direction only. It is an acceptable solution if we allow the beams to be injected separately while adjusting the sextupole strengths accordingly for each of the beam directions.

Alternatively, by incorporating magnetic and electric sextupoles at the same time, the SCT could be improved for both CR beams. The symmetry of the problem (Figs. 10 and 11) shows that CR beams experience the same effect from magnetic and electric sextupoles in case

$$k^m = k_1^m = -k_2^m$$
$$k^e = k_1^e = k_2^e. \tag{10}$$

Hence, having both magnetic and electric sextupoles that follow Eq. (10) will lead to a better SCT for both CR beams—Fig. 12.

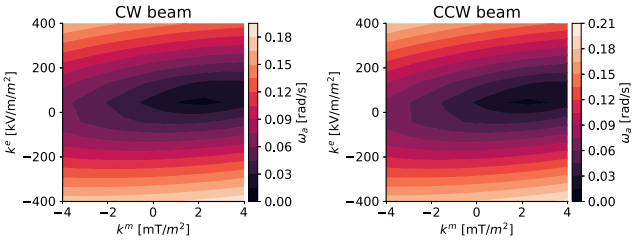

FIG. 12. Single-particle horizontal precession rate ω_a as a function of magnetic and electric sextupole strengths k^m, k^e [Eq. (10)]. Darker: lower ω_a, thus better SCT. Left: CW beam; right: CCW beam. The effect is perfectly symmetric as the variables can only affect CW-CCW beams the same way. Thus, we can improve the SCT for both cases at the same time.

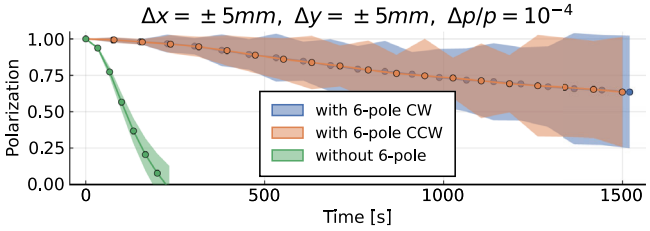

FIG. 13. Magnitude of the polarization vector vs time simulation with a realistic bunch structure given as $\Delta p/p = 10^{-4}$ rms; $\Delta x/x = \pm 5$ mm, $\Delta y/y = \pm 5$ mm as maximum and assuming a uniform phase space distribution. The polarization retains a high value with hybrid (magnetic and electric) sextupoles for both CW (blue) and CCW (orange) bunches compared to the nominal case without sextupoles (green). The estimated SCT is expected to become longer when the betatron amplitudes and momentum exchanges in three dimensions, due to IBS, are taken into account. The simulation is a subsecond long, with the polarization at $t \gg 1$ s estimated by measuring the precession rate for each particle in the simulation, then extrapolated with the corresponding error propagation. Vertical ribbon bands indicate the digitization uncertainty as discussed in Appendix B.

Although the optimal sextupole pair found in Figs. 10–12 is for the reference particle, the same pair happens to be near optimal for the corresponding bunch of particles, too.

By incorporating the best pair k^m and k^e, the SCT improves vastly for both of the CR beams at the same time for a bunch of particles—Fig. 13. Additional details about finding the optimum sextupole strengths are given in Appendix F.

G. Polarimeter systematic issues

Measurement of the proton beam polarization will most likely involve the observation of the asymmetry in the elastic scattering of protons from a light-mass target such as carbon. The differential cross section for protons is given by

$$\sigma(\theta)_{\mathrm{Pol}} = \sigma(\theta)_{\mathrm{UNP}}[1 + pA(\theta)\sin\beta\cos\phi],$$

where θ is the polar scattering angle for the detected protons and β and ϕ are the polar and azimuthal angles for the proton polarization direction (ϕ measured from the perpendicular to the scattering plane). A is the analyzing power, which describes the degree of sensitivity of the scattering to polarization acting through the spin-orbit interaction between the proton and the nucleus. p is the beam polarization. At the energies expected for the EDM search, the small-angle cross section and analyzing power are both large (Fig. 14).

The EDM signal arises from beam polarizations (p) that are perpendicular to the ring plane. These may be detected by comparing the elastic scattering rates on opposite sides of the beam in the ring plane. The $\cos\phi$ azimuthal

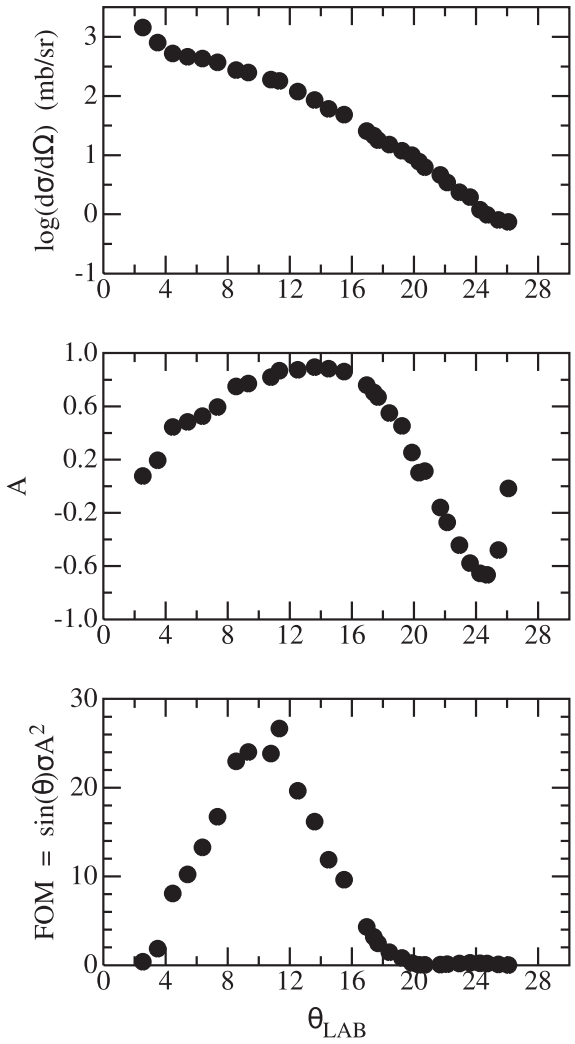

FIG. 14. Angular distributions for elastic proton-carbon scattering at 250 MeV [62] showing the differential cross section, analyzing power, and figure of merit. The figure of merit (FOM) indicates the statistical significance of utilizing parts of the angular distribution in a polarimeter; polar angles between 4° and 16° are optimal.

dependence produces opposite scattering rate changes in these two detectors. If the scattering rates are designated by L and R for the two sides of the beam and measurements are made with both + and − states of the beam polarization, then the vertical component may be determined from

$$\bar{p} = \frac{1}{A}\frac{r-1}{r+1} \qquad r^2 = \frac{L_+ R_-}{L_- R_+}.$$

The combination of simultaneous left- and right-side detection with data using opposite polarization states cancels many first-order errors in this analysis.

Accurately measuring small polarization rotations at the level of microradians means being able to handle errors beyond the first order. To do this, we must create a model of

the terms driving these errors in order to provide a means of making corrections for them in real time if possible. Such a model was created for the original polarimeter used in beam studies at COSY [63]. There must also be parameters that scale the corrections that are themselves sensitive in first order to the driving terms. One such choice is

$$\phi = \frac{s-1}{s+1} \qquad s^2 = \frac{L_+ L_-}{R_+ R_-},$$

which is sensitive to geometric errors in first order but not to the polarization and

$$W = \frac{dL_+}{dt} + \frac{dR_+}{dt} + \frac{dR_-}{dt} + \frac{dL_-}{dt},$$

which is sensitive to the sum of the detector count rates for correcting rate-dependent errors. Next, a calibration must be performed of the sensitivity of the polarimeter to various orders of angle/position errors as a function of these two driving terms. Once in place, monitoring the magnitude of these two terms allows a correction to be made to any polarization observable in real time. This was tested at COSY and proved correct to a level of 10^{-5} (limited by statistics) with no suggestion that the method was encountering a limit.

There are a number of systematic effects that rely on the comparison of asymmetries measured with CR beams. Most likely, this will mean two sets of forward detectors mounted on either side of a single target that is shared by the two beams. For elastic scattering from carbon, backscattering from the target is usually less than 10^{-7} of the forward scattering rate and should not be an issue. But the two polarimeters will be separate instruments, and the calibration of their response to polarization must be precise enough that the difference of the asymmetries they yield is meaningful at the level of 10^{-6}, what is needed for the EDM search.

IV. DISCUSSION AND CONCLUSION

A. Simulation with realistic conditions

We further demonstrate the feasibility of the experiment by including multiple lattice imperfections such as both horizontal and vertical quadrupole misalignments and deflector tilts. All in all, CR beams are required to vertically overlap within $\pm 5\ \mu$m[8] with $\pm 50\ \mu$m overall vertical closed orbit planarity. With such conditions, we first numerically verify that the established realistic conditions are met—Fig. 15. Then, vertical magnetic field B_y and RF cavity frequency are adjusted until no discernible (less than

[8]A much larger beam separation can be tolerated, but 10 μm should be possible to achieve based on technology similar to the SQUID-based beam-position monitors with a resolution of 10 nm/$\sqrt{\text{Hz}}$ [64].

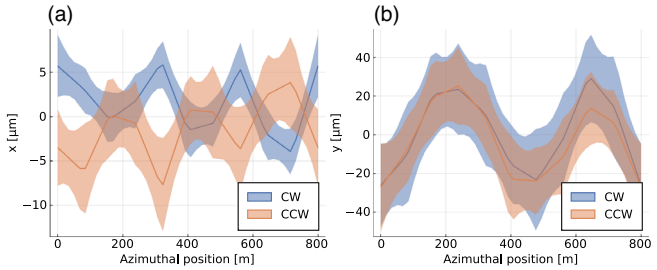

FIG. 15. Single-particle position averaged over 5×10^5 turns split onto 48 bins. (a) Horizontal position throughout the ring azimuth. (b) Vertical position throughout the ring azimuth. Fill color shows standard deviations at the bins, roughly giving an idea about the spread.

$\sim 1\ \mu$rad/s) horizontal spin precession is present. Lastly, we run with both normal and reversed magnetic quadrupole polarities and look at the total EDM signal, which is calculated as in Eq. (C2) below.

Upon examining the result—Fig. 16—it is clear that the unwanted background residual EDM-like signal is below the target experimental sensitivity; hence, the systematic error sources with such lattice alignment requirements are low enough to allow the measurement of the proton EDM to $d < 10^{-29}\ e \cdot$ cm.

B. *B*-field measurement

Although the Symmetric-Hybrid and Hybrid (4-fold) lattice designs completely shield the beam from external magnetic fields, some limits to B fields are necessary due to the maximum beam splitting requirements. This section discusses the technique of measuring the beam splitting, which is also equivalent to measuring the magnetic fields experienced by the CR beams.

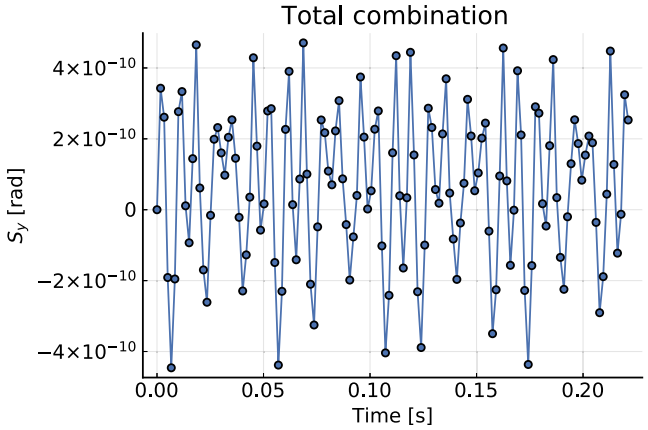

FIG. 16. Vertical spin component S_y vs storage time. The signal comes from calculation of Eqs. (C2) and (C5), with residual EDM-mimicking background precession rate of $dS_y/dt < 1$ nrad/s, which corresponds to the target sensitivity of $d = 10^{-29}\ e \cdot$ cm. The actual numerical vertical spin data oscillates rapidly; hence, it was arbitrarily averaged onto 40 points.

With a specification that the CR beams can split maximum up to ± 5 μm (10 μm in total), only around a sub-nT level B field can be tolerated. This can be achieved by a variety of techniques, one of which is described here. The ring will be surrounded by sets of flux-gate magnetometers and Helmholtz coils to eliminate the external field by active cancellation. The number of sets located around the ring determines the azimuthal B-field harmonics that can be probed and canceled. The magnetic focusing system, if perfectly aligned, does not cause any splitting between the CR beams. Small external magnetic fields are also shielded by the focusing system, as shown in Fig. 8. Since a typical quad field gradient is about 0.2 T/m, even a small quad misalignment will cause a large beam splitting and is expected to be the dominant source of the beam separation around the ring.

The split can be measured by means of magnetic pickups. A micrometer-level vertical split induces roughly pico Tesla (pT)-level radial magnetic field at a few centimeters distance from the beam [64], due to the CR beams. To increase the signal-to-noise ratio, the quadrupole fields will be modulated at 1–10 kHz by 1%, which is coined as K-modulation [65]. The measurement can be easily accomplished with commercially available flux-gate magnetometers (with a few $\mathrm{pT}/\sqrt{\mathrm{Hz}}$ sensitivity) operating at room temperature, while there are a variety of other commercial options as well. A recently developed SQUID-based beam position monitor (BPM) has a potential to measure the split with better than 10 $\mathrm{fT}/\sqrt{\mathrm{Hz}}$ sensitivity [64].

C. Experimental knobs

In this section, a brief summary of the available experimental knobs that reduce the effects of systematic error sources is listed. Methods unused in this study are marked and will require additional detailed studies:

(i) *CR beam storage*.—Simultaneous CR beam storage eliminates a whole class of systematic error sources, including the dipole (and higher odd multipoles of) E field, the Earth's gravitation field, and some additional geometrical phases (Appendix E).

(ii) *Quadrupole polarity switching*.—As mentioned in Appendix C, flipping the polarity of the magnetic quadrupoles effectively phase shifts the beta functions. Therefore, a significant amount of systematic error sources that depend on local values of the beta function are suppressed.

(iii) *Beam splitting*.—Applying radial and vertical magnetic fields $B_{x,y}$ to split the CR beams enhances the effect of local (skew) quadrupole E fields (Sec. III C). Splitting the CR beams increases local beam offsets that will greatly amplify effects of quadrupole and higher-order E fields. With such amplification, it is possible to measure and control high order E fields via SBA.

(iv) *Positive and negative helicities*.—Probing EDM. In addition to CR beam storage, bunches with opposite helicities are present, too, reserved for polarimeter related systematics.

(v) *Radially polarized bunches*.—Probing DM/DE. Radially polarized bunches are the most sensitive to the vertical velocity effect (Sec. III A) and some additional geometrical phases (Appendix E). Radially polarized bunches are needed for SBA and also used for the data combination (Appendix C).

(vi) *Vertically polarized bunches*.—Probing simultaneously EDM and DM/DE. Currently, only radially and longitudinally polarized beams were considered. Utilizing spin precession data of vertically polarized beams could be used to further mitigate systematic error sources. Vertically polarized bunches are sensitive to different $\vec{\Omega}_a$ components, which could be used to isolate the EDM component even better (unused in this study).

(vii) *Quadrupole strength variation*.—Having been proposed first in Ref. [38], varying the quadrupole strengths lets us extrapolate the effective vertical spin precession rate at an infinite quadrupole strength by subsequently increasing the focusing gradient k, where the beam split is minimal (unused in this study).

(viii) *Polarization measurement*.—Every few seconds, the spin direction will be rotated around the vertical axis in one direction and immediately in the opposite one, in order to have an accurate measurement of the beam polarization value as well as of the vertical spin component as a function of time. This technique is implicitly assumed in this work.

D. Conclusion

The most important systematic error sources in the storage ring proton EDM experiment are covered. Overall, we have shown that for the specified ring alignment requirements the most significant systematic error sources are well below the target EDM sensitivity. This paper has introduced novel methods of improving the sensitivity of the experiment such as Symmetric-Hybrid ring design, hybrid sextupoles for increased SCT, and spin-based alignment. Combined with Refs. [34,38,42], this work aims to be the constitutive basis for the conceptual and technical design reports. We expect to write a white paper as part of the current community effort to evaluate its options and set the priorities for the next five years. Assuming a positive outcome, a CDR is in order, with a parallel effort of a "string test" including all the hardware, plus the injection system, of 1/48th of the ring lattice. The purpose would be to test compatibility and cross-interactions, after which we will finalize the hardware specifications and the technical design report.

ACKNOWLEDGMENTS

This work was supported by Grant No. IBS-R017-D1 Republic of Korea; U.S. Department of Energy under Grant No. DE-SC0012704; U.S. Department of Energy, Office of Science, Office of Nuclear Physics under Contract No. DE-AC05-06OR23177; and Grant No. 2019VMA0019 of CAS President's International Fellowship Initiative.

APPENDIX A: ELECTRODE MATERIAL AND DESIGN

The ring design imposes strict requirements on the choice of the electrode material. The electrodes must be compatible with bakeout at 200 °C (due to required vacuum of 10^{-10} torr) and nonmagnetic since the background magnetic field must be very small (<1 nT). Other requirements relate to having an electrode made of a material that is easy to machine and polish. The electrode must also be made to very good tolerances to meet the required alignment and be from a light weight material. From the many choices considered [66,67], stainless steel 316 L, niobium, molybdenum, titanium, and TiN-coated aluminum show great promise.

The studies done on TiN-coated small electrodes [67], where the aluminum electrodes were manufactured from Al6061 alloy, required only hours of mechanical polishing using silicon carbide paper. The coating was about 2.5 μm thick, and the electrodes were baked at 200 °C for 30 h and achieved 10^{-11} torr. However, these were small electrodes, and coating large pieces will be a challenge. Although the tested small pieces did not show field emission up to 14 MV/m, it is known that large pieces will not perform as well as small pieces.

Table V shows the properties of a single electrode plate. The ring will use 1152 such plates. The transverse edges of these plates can be shaped with Rogowski edge profile and electrostatic modeled to find the maximum field strength. The model will also speak to field strength everywhere inside the vacuum pipe and not just between the plates. To bias the plates and support them inside the vacuum pipe, one can use inverted insulators. R24 insulators should work as they are relatively compact, about 10 cm long, and rated to nearly 200 kV. Each plate will be supported by two insulators. Since these insulators are sold to the medical x-ray community, they should be relatively inexpensive.

TABLE V. Properties of a single electrode plate.

Length	104 cm
Electrode height	20.0 cm
Gap width	4.0 cm
Bending field	4.391 MV/m
Maximum field	To be modeled
Voltage per plate	±87.82 kV
Bending radius	95.49 m

There are industry standard cables with R24 connectors. Small alumina insulator spacers can be used to hold the plates apart and provide a relatively accurate gap. These spacers would also minimize bowing due to electrostatic forces. However, the design should prevent line of sight, to avoid the possibility of charging up these spacers, and confirm that these small insulator spacers will not distort the field homogeneity. The spacers would simplify construction and minimize expense of *in situ* alignment. All triple-point junctions (wherever metal touches insulator in vacuum) could be a source of high-voltage breakdown and requires careful design and shielding [68].

For each electrode with dimensions roughly 104 cm long by 20 cm tall by 4 cm thick, the total volume is 8320 cm^3. Given aluminum density of 2.7 g/cm^3, each electrode weighs roughly 22 kg (or 50 lb). To reduce weight and cost, hollow aluminum electrodes should be considered. One way to mount the electrodes inside the beam pipe is to have the insulators oriented vertically, supporting the plates from below, with gravity helping. However, this breaks the vertical symmetry and may introduce a vertical electric field component. In this case, the electrodes should be mounted from the back side.

To apply high voltage of each polarity, the plates can be daisy chained together with one supply biasing many plates. Additionally, the high-voltage system should be configured such that plates can be biased separately, and negatively with the other plate grounded, to allow gas conditioning when field emission is observed. Effects of high-voltage stability and ripple should be investigated.

Since the vertical electric field, E_y, and its stability are the main systematic uncertainties in the experiment, one must consider very carefully the mechanical alignment of the electrode plates; the flatness of the aluminum plates; polishing and coating, especially such large pieces; and electrode plates parallelism. In principle, not only for the plates but also the insulators, with such a large number of insulators needed, the required tolerances on manufacturing of these has to be also specified.

APPENDIX B: EXTRACTION OF THE LINEAR RATE FROM A NOISY CURVE

Measuring the rate (slope) of a linear curve under random noise can only be done up to some certain statistical significance. For example, the random linear $x - y$ curve given in Fig. 17 (bottom left column) is subjected to random normal increasing-in-magnitude noise (mid-top left column). Although there are a few possibilities to extract the underlying rate (slope), in this work, the data are averaged onto two points with the standard deviations noted—Fig. 17 (right column). Next, a least-squares fit is performed to assess the slope and the standard error of the slope.

With the obtained estimate of the underlying rate, analogous to estimation of the vertical spin precession

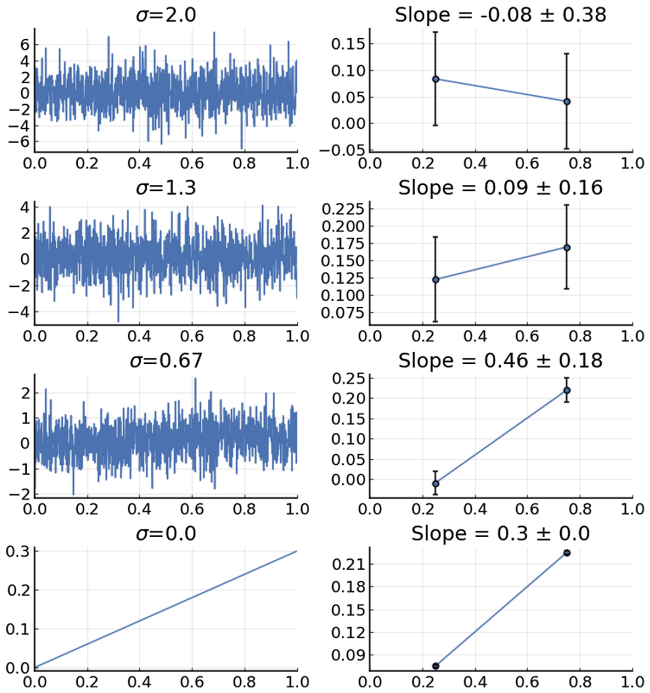

FIG. 17. Left column: random data with an increasing amount of normally distributed noise with σ. The underlying data (last row) have no noise ($\sigma = 0$) width with its true slope apparent. With increasing noise levels (first three rows), the same slope becomes hidden due to large noise. The data contain 1000 points. Right column: The data from the corresponding rows of the left column are averaged into two bins. The error bar assigned to each of the two bins is standard deviation$/\sqrt{n}$.

rate, a confidence interval is reported as the maximal possible rate. Because of such statistical uncertainty (not numerical uncertainty), low precession rate values happen to be irregular—Figs. 6–8. The simulation is unable to achieve times of order of 1000 s (real experiment) under reasonable time and precision requirements. Hence, it has been performed such that the random noise in the vertical spin component due to free betatron and spin oscillations does not contribute more than the target precision level of 10^{-9} rad/s.

APPENDIX C: DATA COMBINATION

Out-of-plane precession direction due to a genuine EDM signal would be opposite for positive helicity CR beams in the same storage ring. Namely,[9]

$$\left(\frac{dS_y}{dt}\right)_{\mathrm{EDM}} = \frac{1}{2}\left(\frac{dS_y}{dt}\right)_{\mathrm{CW}} - \frac{1}{2}\left(\frac{dS_y}{dt}\right)_{\mathrm{CCW}} \tag{C1}$$

vertical spin precession due to the EDM is the difference of the vertical precessions of CW and CCW beams, with a factor of 1/2 to compensate for the doubling of the true EDM signal.

Complementing the simultaneous storage of CR beams, we can have another symmetrical flip—polarity switch. It is the act of switching the direction of the currents in the magnetic quadrupoles. Quadrupoles being maximally current dominated makes it possible to phase shift the lattice beta functions by reversing direction of the currents in all the magnetic quadrupoles. Then, the EDM signal is given as

$$\left(\frac{dS_y}{dt}\right)_{\mathrm{EDM}} = \left[\frac{1}{4}\left(\frac{dS_y}{dt}\right)_{\mathrm{CW}} - \frac{1}{4}\left(\frac{dS_y}{dt}\right)_{\mathrm{CCW}}\right]_{\mathrm{Polarity\ 1}} + \left[\frac{1}{4}\left(\frac{dS_y}{dt}\right)_{\mathrm{CW}} - \frac{1}{4}\left(\frac{dS_y}{dt}\right)_{\mathrm{CCW}}\right]_{\mathrm{Polarity\ 2}}. \tag{C2}$$

In addition to the polarity switch of the quadrupoles, one can choose to change the quadrupole gradient k to extract $dS_y/dt \propto 1/k$ in the asymptotic limit of $1/k \to 0$ as was first suggested in Ref. [38].

In addition to the vertical spin precession, the spin would also (inevitably) precess into radial direction, assuming the lattice conditions listed in Sec. IV A. Radial spin precession could create a vertical precession (Sec. III A).

We can model this case analytically and compensate for such radial spin precession. We denote the vertical spin precession rate as the combined effect from both radial and longitudinal polarizations,

$$\frac{dS_y}{dt} = \eta' S_s + \delta' S_x. \tag{C3}$$

η' indicates EDM-like precession that only happens due to a longitudinal spin component S_s, and δ' indicates dark-matter-like precession that happens due to a radial spin component S_x. η' and δ' show only the combined background effect. For example, δ' directly contains the vertical velocity and other systematics that only happen when the spin is radial.

Assuming that an initially longitudinally polarized bunch precesses into radial direction linearly with time,

$$\frac{dS_x}{dt} = \Gamma S_s, \tag{C4}$$

where Γ stands for $(g-2)$—like in-plane spin precession.

If the radial and vertical spin precession rates are small, i.e., $1 \approx S_s \gg S_x, S_y$ at all times, the coupled differential equations [Eqs. (C3) and (C4)] have the solution

$$S_s \eta' = \frac{d}{dt}(S_y - \delta' \Gamma t^2 S_s/2). \tag{C5}$$

The quadratic in time behavior caused by the drift into radial spin direction is confirmed—Fig. 18.

[9] y is vertical in the laboratory frame.

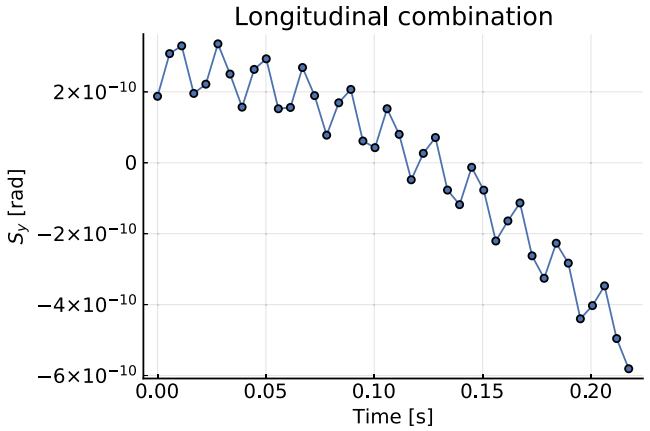

FIG. 18. Effective vertical spin component precession data of CW-CCW and both quadrupole polarities calculated from Eq. (C2). The quadratic behavior of this curve is explained by Eq. (C5).

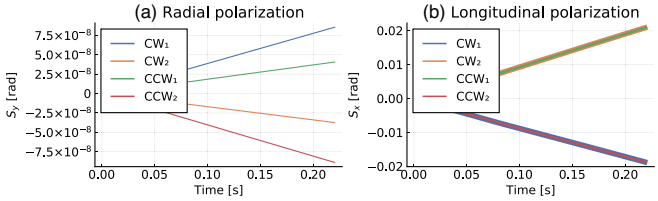

FIG. 19. (a) Vertical spin precession of a radially polarized beam for all beam directions and polarities (subscripts). Main contribution of the spin growth originates from vertical velocity effect Sec. III A. (b) Radial spin precession of a longitudinally polarized beam for all beam directions and polarities (subscripts). The spin precesses into radial direction due to RF frequency mismatch and nonzero average B_y present in the storage ring due to the misalignment of magnetic quadrupoles.

First, δ' and Γ are estimated from spin precession data—Fig. 19. After redefining the effective $\frac{dS_y}{dt}$ as

$$\frac{dS_y}{dt} \leftarrow \frac{d}{dt}(S_y - \delta'\Gamma t^2 S_s/2),$$

η' can now be correctly estimated with Eqs. (C2) and (C5). The total combination result is given in Fig. 16, from which it is clear that $\eta' < 1$ nrad/s.

APPENDIX D: HIGH-PRECISION TRACKING

The Lorentz equation governs the dynamics of a particle in EM fields,

$$\frac{d\vec{\beta}}{dt} = \frac{q}{m\gamma c}[\vec{E} + c\vec{\beta} \times \vec{B} - \beta(\vec{\beta} \cdot \vec{E})].$$

However, its perturbative expansion in particle optical coordinates is more practical for storage rings and accelerators, as we are using natural variables of interest [69],

$$\begin{aligned}
x' &= a(1+hx)\frac{p_0}{p_s} \\
a' &= (1+hx)\left[\frac{\gamma}{\gamma_0}\frac{E_x}{\chi_{e0}}\frac{p_0}{p_s} + b\frac{B_s}{\chi_{m0}}\frac{p_0}{p_s} - \frac{B_y}{\chi_{m0}}\right] + h\frac{p_s}{p_0} \\
y' &= b(1+hx)\frac{p_o}{p_s} \\
b' &= (1+hx)\left[\frac{\gamma}{\gamma_0}\frac{E_y}{\chi_{e0}}\frac{p_0}{p_s} + \frac{B_x}{\chi_{m0}} - a\frac{B_s}{\chi_{m0}}\frac{p_0}{p_s}\right],
\end{aligned}$$

where the prime indicates differentiation with respect to s (beamline travel distance) and subscript 0 is the quantity with respect to the reference particle. In this curvilinear (Frenet-Serret) coordinate system, x indicates radial deviation from the reference orbit, y indicates vertical deviation, and s points along the direction of motion of the reference particle. Hence, the momentum in this coordinate system is measured in $\vec{p}/p_0 = (a, b, p_s/p_0)$. $h = 1/R_0$ indicates curvature for the reference orbit and $\chi_{e0}, \chi_{m0} = p_0 v/Ze,\ p_0/Ze$ the electric and magnetic rigidities.

The spin vector should then be integrated with the T-BMT equation [39,40] given in Cartesian coordinates as follows:

$$\frac{d\vec{S}}{dt} = \vec{\Omega} \times \vec{S}$$

$$\begin{aligned}
\frac{d\vec{S}}{dt} = \frac{q}{m}\vec{S} \times \Bigg[&\left(a + \frac{1}{\gamma}\right)\vec{B} - \frac{a\gamma}{\gamma+1}\vec{\beta}(\vec{\beta}\cdot\vec{B}) \\
&- \left(a + \frac{1}{\gamma+1}\right)\frac{\vec{\beta}\times\vec{E}}{c} \\
&+ \frac{\eta}{2}\left(\frac{\vec{E}}{c} - \frac{\gamma}{\gamma+1}\frac{\vec{\beta}}{c}(\vec{\beta}\cdot\vec{E}) + \vec{\beta}\times\vec{B}\right)\Bigg].
\end{aligned} \tag{D1}$$

The spin is normalized to unity and needs to be measured in terms of $\vec{S} = (S_x, S_y, S_s)$—radial, vertical, and longitudinal spin components for convenience. Such deviation from Cartesian coordinates needs appropriate modification to the original T-BMT equation [Eq. (D1)] as,

$$\vec{S}' = (\vec{\Omega}t' - h\hat{y}) \times \vec{S} \tag{D2}$$

in order to compensate for the rotation of the coordinate system itself and take into account that we want the derivative with respect to the s integration variable (here, $\hat{y}$ refers to the vertical—out-of-the-plane—unit vector).

Each of the storage ring elements has been tracked separately in order to avoid discontinuities in EM fields that directly lead to unstable numerical integration. Electric

bending plates were hard-edge approximated. The fields inside cylindrical deflectors with a focusing index $n = m + 1$ are given as [70,71]

$$E_x = -E_0\left(1 - \frac{nx}{R_0} + \frac{n(n+1)x^2}{2R_0^2}\right)$$
$$E_y = -E_0\left((n-1)\frac{y}{R_0}\right).$$

It is important to note that, in order to meet the precision requirements, second-order terms (x^2) must be considered to have precise spin integration.

APPENDIX E: DETAILED ANALYSIS OF THE GEOMETRICAL PHASES

The terms in the T-BMT equation proportional to the E field are the main mechanism for systematic error sources, as B fields are naturally shielded by the quadrupoles. In addition to the dipole E field, vertical velocity, and quadrupole E field (Secs. III B and III C), there exist additional ways of creating background vertical spin precession.

The list of the possible terms from Eq. (D1) is given below (in the order of importance attributed by us):

(1) $dS_y/dt \propto S_x \cdot \beta_y \cdot E_x$, discussed in Sec. III A, also recognized as "twist" distortion.
(2) $dS_y/dt \propto S_s \cdot \beta_s \cdot E_y$, discussed in Sec. III B.
(3) $dS_y/dt \propto S_s \cdot \beta_y \cdot E_s$, which will receive additional treatment in this section.
(4) $dS_y/dt \propto S_x \cdot \beta_x \cdot E_y$, which will receive additional treatment in this section.

The $dS_y/dt \propto S_s \cdot \beta_y \cdot E_s$ term directly couples to the longitudinal polarization (EDM search); thus, circumventing its effect via SBA is not trivial. As it has been argued in Sec. III A, the average effect of the $S_s \cdot \beta_y \cdot E_s$ term would not be zero. Nevertheless, from an energy conservation stand point, $\int E_s ds = 0$ per each deflector. A static electric field cannot induce a net acceleration (or deceleration) on a passing particle. Hence, the effect of this term effectively applies to nonstatic longitudinal electric fields. High-precision numerical spin tracking has shown that, even in the case where $\int E_s ds \neq 0$, for example, due a changing-in-time magnetic flux through the storage ring plane, the resulting false EDM signal is below 1 nrad/s for fields $E_s <$ 5 V/m normally distributed along the ring azimuth.

The $dS_y/dt \propto S_x \cdot \beta_x \cdot E_y$ term couples to the radial polarization, and hence the effect is suppressed via SBA (Sec. III C). Isolation of this effect is challenging, as its contribution is orders of magnitude below the vertical velocity effect. A vertical velocity is inadvertently created when probing for the $S_x \cdot \beta_x \cdot E_y$ effect, as $E_y \neq 0$ fields create $\beta_y \neq 0$. This effect is negligible for the current sensitivity goals and could be ignored for all practical purposes.

APPENDIX F: OPTIMUM SEXTUPOLE STRENGTH SEARCH

In Figs. 10–12, the optimal sextupole strengths pair is obtained by a rough two-dimensional parameter sweep, followed by numerical optimization to find the finer minimum. It is worthwhile to show that finding the optimal pairs for magnetic and electric sextupoles separately is sufficient to infer the value for the optimum strength needed for hybrid sextupoles.

Let us suppose that $k_1^m = \alpha_1, k_2^m = -\beta_1$ is the optimal pair for magnetic sextupoles for CW beam, with $k_1^m = \beta_1, k_2^m = -\alpha_1$ for the CCW case. Similarly, $k_1^e = -\alpha_2, k_2^e = \beta_2$ and $k_1^e = \beta_2, k_2^e = -\alpha_2$ for the CW and CCW directions, respectively, with electric sextupoles.

By observing the symmetry in Figs. 10 and 11, we can infer that

$$k_1^m = -\frac{\alpha_1}{\alpha_2} \times k_1^e \qquad k_2^m = -\frac{\beta_1}{\beta_2} \times k_2^e \quad \text{for CW} \tag{F1}$$

$$k_1^m = \frac{\beta_1}{\beta_2} \times k_1^e \qquad k_2^m = \frac{\alpha_1}{\alpha_2} \times k_2^e \quad \text{for CCW;} \tag{F2}$$

i.e., only a sign change is required for the transition from electric to magnetic or vice versa. We can also infer the conversion factor from electric to magnetic sextupoles. Following the lines of the symmetry, we can find the optimal pair for the hybrid sextupoles case in magnetic units,

$$M_1 + E_1 = \alpha_1 \qquad -M_1 + E_1 = -\beta_1, \tag{F3}$$

and solving for each $M_1 = (\alpha_1 + \beta_1)/2$ and $E_1 = \alpha_2/\alpha_1 \times (\alpha_1 - \beta_1)/2$, we get the optimal pair for each case in proper units. Figures 10–12 verify these analytical estimations to 1% accuracy.

[1] B. Abi *et al.* (Muon $g-2$ Collaboration), Phys. Rev. Lett. **126**, 141801 (2021).
[2] T. Albahri *et al.* (Muon $g-2$ Collaboration), Phys. Rev. D **103**, 072002 (2021).
[3] T. Albahri *et al.* (Muon $g-2$ Collaboration), Phys. Rev. Accel. Beams **24**, 044002 (2021).
[4] T. Albahri *et al.* (The Muon $g-2$ Collaboration), Phys. Rev. A **103**, 042208 (2021).

[5] M. Pospelov and A. Ritz, Ann. Phys. (Amsterdam) **318**, 119 (2005).
[6] J. Engel, M. J. Ramsey-Musolf, and U. van Kolck, Prog. Part. Nucl. Phys. **71**, 21 (2013).
[7] T. Chupp, P. Fierlinger, M. Ramsey-Musolf, and J. Singh, Rev. Mod. Phys. **91**, 015001 (2019).
[8] R. J. Crewther, P. Di Vecchia, G. Veneziano, and E. Witten, Phys. Lett. **88B**, 123 (1979); **91B**, 487(E) (1980).
[9] E. Mereghetti, J. de Vries, W. H. Hockings, C. M. Maekawa, and U. van Kolck, Phys. Lett. B **696**, 97 (2011).
[10] J. Dragos, T. Luu, A. Shindler, J. de Vries, and A. Yousif, Phys. Rev. C **103**, 015202 (2021).
[11] T. Izubuchi, H. Ohki, and S. Syritsyn, *Proc. Sci.*, LATTICE2019 (2020) 290 [arXiv:2004.10449].
[12] T. Bhattacharya, V. Cirigliano, R. Gupta, E. Mereghetti, and B. Yoon, arXiv:2101.07230.
[13] C. Abel *et al.*, Phys. Rev. Lett. **124**, 081803 (2020).
[14] S. Drury, T. Blum, M. Hayakawa, T. Izubuchi, C. Sachrajda, and R. Zhou, Proc. Sci., LATTICE2013 (**2014**) 268 [arXiv:1312.0477].
[15] A. Bazavov *et al.* (Fermilab Lattice, MILC, and TUMQCD Collaborations), Phys. Rev. D **98**, 054517 (2018).
[16] C. Alexandrou, J. Finkenrath, L. Funcke, K. Jansen, B. Kostrzewa, F. Pittler, and C. Urbach, Phys. Rev. Lett. **125**, 232001 (2020).
[17] R. D. Peccei and H. R. Quinn, Phys. Rev. Lett. **38**, 1440 (1977).
[18] R. D. Peccei and H. R. Quinn, Phys. Rev. D **16**, 1791 (1977).
[19] S. Weinberg, Phys. Rev. Lett. **40**, 223 (1978).
[20] F. Wilczek, Phys. Rev. Lett. **40**, 279 (1978).
[21] M. Tanabashi *et al.* (Particle Data Group), Phys. Rev. D **98**, 030001 (2018).
[22] A. Sakharov, Sov. Phys. Usp. **34**, 392 (1991).
[23] T. Golling *et al.*, arXiv:1606.00947.
[24] R. Essig *et al.*, in *Community Summer Study 2013: Snowmass on the Mississippi* (2013), https://arxiv.org/abs/1311.0029.
[25] M. Battaglieri *et al.*, in *U.S. Cosmic Visions: New Ideas in Dark Matter* (2017), https://arxiv.org/abs/1707.04591.
[26] S. Tulin, Phys. Rev. D **89**, 114008 (2014).
[27] J. A. Dror, R. Lasenby, and M. Pospelov, Phys. Rev. Lett. **119**, 141803 (2017).
[28] P. Ilten, Y. Soreq, M. Williams, and W. Xue, J. High Energy Phys. 06 (2018) 004.
[29] G. W. Bennett *et al.*, Phys. Rev. D **73**, 072003 (2006).
[30] T. Aoyama *et al.*, Phys. Rep. **887**, 1 (2020).
[31] Sz. Borsanyi *et al.*, Nature (London) **593**, 51 (2021).
[32] G. W. Bennett *et al.* (Muon $(g-2)$ Collaboration), Phys. Rev. D **80**, 052008 (2009).
[33] V. Anastassopoulos *et al.*, AGS proposal: Search for a permanent electric dipole moment of the deuteron nucleus at the 10^{-29} $e\cdot$cm level, access: 2008, https://www.bnl.gov/edm/files/pdf/deuteron_proposal_080423_final.pdf.
[34] V. Anastassopoulos *et al.*, Rev. Sci. Instrum. **87**, 115116 (2016).
[35] M. Plotkin, The Brookhaven electron analogue, 1953–1957, Technical Report, Brookhaven National Lab., Upton, NY (United States), 1991 (Note: Brookhaven National Laboratory built a 10 MeV all-electric electron storage ring in the 1950s to do studies in preparaton for the 30 GeV AGS. It could not use protons because of intrabeam scattering. An all-electric ring was cheaper and easier to build compared to a magnetic ring, if the laboratory had enough space, which it did), https://www.osti.gov/biblio/5629527.
[36] S. Hacıömeroğlu, Y. F. Orlov, and Y. K. Semertzidis, Nucl. Instrum. Methods Phys. Res., Sect. A **927**, 262 (2019).
[37] P. W. Graham, S. Hacıömeroğlu, D. E. Kaplan, Z. Omarov, S. Rajendran, and Y. K. Semertzidis, Phys. Rev. D **103**, 055010 (2021).
[38] S. Hacıömeroğlu and Y. K. Semertzidis, Phys. Rev. Accel. Beams **22**, 034001 (2019).
[39] V. Bargmann, L. Michel, and V. L. Telegdi, Phys. Rev. Lett. **2**, 435 (1959).
[40] T. Fukuyama and A. J. Silenko, Int. J. Mod. Phys. A **28**, 1350147 (2013).
[41] A. J. Silenko, Phys. Rev. ST Accel. Beams **9**, 034003 (2006).
[42] V. Anastassopoulos *et al.*, A proposal to measure the proton electric dipole moment with 10^{-29} $e\cdot$cm sensitivity, by the Storage ring EDM collaboration, accessed: 2011, https://inspirehep.net/files/fedd912e77ee5f1defd288d2ea8f8aeb.
[43] F. J. M. Farley, K. Jungmann, J. P. Miller, W. M. Morse, Y. F. Orlov, B. L. Roberts, Y. K. Semertzidis, A. Silenko, and E. J. Stephenson, Phys. Rev. Lett. **93**, 052001 (2004).
[44] A. Mooser, S. Ulmer, K. Blaum, K. Franke, H. Kracke, C. Leiteritz, W. Quint, C. C. Rodegheri, C. Smorra, and J. Walz, Nature (London) **509**, 596 (2014).
[45] C. Tsitouras, Comput. Math. Appl. **62**, 770 (2011).
[46] M. V. Berry, Proc. R. Soc. A **392**, 45 (1984).
[47] C. A. Baker, D. D. Doyle, P. Geltenbort, K. Green, M. G. D. van der Grinten, P. G. Harris, P. Iaydjiev, S. N. Ivanov, D. J. R. May, J. M. Pendlebury, J. D. Richardson, D. Shiers, and K. F. Smith, Phys. Rev. Lett. **97**, 131801 (2006).
[48] J. M. Pendlebury, W. Heil, Y. Sobolev, P. G. Harris, J. D. Richardson, R. J. Baskin, D. D. Doyle, P. Geltenbort, K. Green, M. G. D. van der Grinten, P. S. Iaydjiev, S. N. Ivanov, D. J. R. May, and K. F. Smith, Phys. Rev. A **70**, 032102 (2004).
[49] A. J. Silenko, Nonlinear Phenom. Complex Syst. **20**, 347 (2017), http://www.j-npcs.org/abstracts/vol2017/v20no4/v20no4p347.html.
[50] B. Yangand and H. Friedsam, Phys. Rev. ST Accel. Beams **9**, 030701 (2006).
[51] V. Shiltsev, Phys. Rev. ST Accel. Beams **13**, 094801 (2010).
[52] A. J. Silenko, Phys. Rev. D **93**, 124050 (2016).
[53] Y. N. Obukhov, A. J. Silenko, and O. V. Teryaev, Phys. Rev. D **94**, 044019 (2016).
[54] Y. N. Obukhov, A. J. Silenko, and O. V. Teryaev, Phys. Rev. D **96**, 105005 (2017).
[55] A. J. Silenko and O. V. Teryaev, Phys. Rev. D **76**, 061101(R) (2007).
[56] Y. Orlov, E. Flanagan, and Y. Semertzidis, Phys. Lett. A **376**, 2822 (2012).
[57] A. László and Z. Zimborás, Classical Quantum Gravity **35**, 175003 (2018).
[58] S. Vergeles and N. Nikolaev, J. Exp. Theor. Phys. **129**, 541 (2019).

[59] I. B. Vasserman, P. V. Vorobyov, E. S. Gluskin, P. M. Ivanov, I. A. Koop, G. Y. Kezerashvili, A. P. Lysenko, I. N. Nesterenko, E. A. Perevedentsev, A. A. Mikhailichenko, A. A. Polunin, S. I. Serednyakov, A. N. Skrinsky, and Yu. M. Shatunov, Phys. Lett. B **198**, 302 (1987).

[60] I. Koop and J. M. Shatunov, in *European Particle Accelerator Conference* (1988), https://inis.iaea.org/search/search.aspx?orig_q=RN:23019514.

[61] G. Guidoboni *et al.* (JEDI Collaboration), Phys. Rev. Lett. **117**, 054801 (2016).

[62] H. O. Meyer, P. Schwandt, R. Abegg, C. A. Miller, K. P. Jackson, S. Yen, G. Gaillard, M. Hugi, R. Helmer, D. Frekers *et al.*, Phys. Rev. C **37**, 544 (1988).

[63] N. Brantjes, V. Dzordzhadze, R. Gebel, F. Gonnella, F. Gray, D. Van der Hoek, A. Imig, W. Kruithof, D. Lazarus, A. Lehrach *et al.*, Nucl. Instrum. Methods Phys. Res., Sect. A **664**, 49 (2012).

[64] S. Haciomeroglu, D. Kawall, Y.-H. Lee, A. Matlashov, Z. Omarov, and Y. K. Semertzidis, *The 39th International Conference on High Energy Physics*, ICHEP2018 (Proceedings of science, 2018), https://pos.sissa.it/340/279/.

[65] P. Tenenbaumand and T. Raubenheimer, Phys. Rev. ST Accel. Beams **3**, 052801 (2000).

[66] M. BastaniNejad, Md. A. Mohamed, A. A. Elmustafa, P. Adderley, J. Clark, S. Covert, J. Hansknecht, C. Hernandez-Garcia, M. Poelker, R. Mammei, K. Surles-Law, and P. Williams, Phys. Rev. ST Accel. Beams **15**, 083502 (2012).

[67] Md. A. A. Mamun, A. A. Elmustafa, R. Taus, E. Forman, and M. Poelker, J. Vac. Sci. Technol. A **33**, 031604 (2015).

[68] G. Palacios-Serrano, F. Hannon, C. Hernandez-Garcia, M. Poelker, and H. Baumgart, Rev. Sci. Instrum. **89**, 104703 (2018).

[69] M. Berz, *An Introduction to Beam Physics*, 1st ed. (CRC Press, Boca Raton, 2014).

[70] E. M. Metodiev, K. L. Huang, Y. K. Semertzidis, and W. M. Morse, Phys. Rev. ST Accel. Beams **17**, 074002 (2014).

[71] E. M. Metodiev, I. M. D'Silva, M. Fandaros, M. Gaisser, S. Hacıömeroğlu, D. Huang, K. L. Huang, A. Patil, R. Prodromou, O. A. Semertzidis, D. Sharma, A. N. Stamatakis, Y. F. Orlov, and Y. K. Semertzidis, Nucl. Instrum. Methods Phys. Res., Sect. A **797**, 311 (2015).